

Responses to reviewer 2

Manuscript No.: SE-2019-8

Reviewer 2: In this work, the author uses a multiple-scattering approach to infer the source spectra of small to moderate earthquakes recorded in central Anatolia using the observed energy envelopes of seismograms. The method, originally developed by Sens-Schoenfelder and Wegler (2006), is based on isotropic, scalar radiative transfer theory and makes use of a generalized inversion technique. The author obtains source spectra that are generally well fitted by the classical omega-squared source spectrum for the largest one. For smaller events, there is considerably more scatter in the exponent of the spectral decay at high frequency. The author shows that there exists a reasonably good correspondence between the local Magnitude M_L and the coda-derived moment magnitude. I think that the study confirms the overall interest in using coda waves to study the source of small earthquakes. It also suggests that the physics of smaller events might be different from the one of larger earthquakes. The analysis is sound and the study will be useful to convert local magnitudes to moment magnitudes in future investigations of the area. Therefore, I support the publication of the manuscript after the following questions/points have been addressed.

T.E: I appreciate for your very detailed reading and for positive encouraging opinion now about this study. The annotated text that you provided as supplementary figure among your revision process was too helpful in improving the text since I could correct several typos, rephrase unclear statements in this way. Below you can find my opinion corresponding to the issues you have raised and necessary corrections based on your comments. I have highlighted all changes in red color in the main text.

Reviewer 2: In introduction, I would suggest to distinguish more clearly between parametric approaches (such as the one developed by Mayeda and co-workers) and physics-based approaches (Wegler and co-workers). In the present version, what distinguishes the two methods is not really clear.

T.E.: We are thankful the reviewer for his careful reading this part. We can understand unclear points and performed some modification to enhance this part of the text.

Reviewer 2: It is written that the method of Wegler does not rely on coda normalization. I think that this is an overstatement: although the authors do not explicitly “coda-normalize” their data, I still think that the separation of source and site effects still relies heavily on the fact that at long lapse-time in the coda, the energy distribution homogenizes spatially. If I am mistaken, please explain why.

T.E.: Reviewer is partly correct because usually coda-normalization may fail for smaller events since the use of shorter coda waves in this case does not satisfy the requirement of homogeneous distribution of energy in space. This is mainly due to the fact that the presence of random seismic noise can dominate coda part. We avoid such shortcoming by involving source excitation and site amplification terms directly in the inversion process.

Reviewer 2: I would recommend to split section 2 into two sections: Geology on the one hand and Data on the other hand.

T.E.: I implemented this suggestion. Additionally, based on the suggestion of reviewer 1, I shortened the geology section by leaving out redundant amount of knowledge in this section.

Reviewer 2: In the data section, it would be useful to state the final number of utilized paths after applying the selection criteria for the coda.

T.E.: This information is now added into the Data section.

Reviewer 2: In the Method section, there are a few typos in the Eqs, please verify. I would recommend to explain how g is updated in the inversion process. Furthermore, I think that it would be useful to discuss the possible trade-offs among the unknown in the system of Eqs (4).

T.E.: I thank reviewer 2 for his highlighting a few typos in related equations. They are corrected now. In a response to the reviewer #1, I have added analytical expression of Green's function to clarify its dependence on the scattering attenuation parameter g . I explain the stepwise procedure about how the parameter g is updated between lines # 212-218 (new manuscript). However, I should also notice that preferred to give a summarized version of the inversion strategy in this manuscript and tried to avoid going into too many details about attenuation parameter estimation in the manuscript mainly since the current work is just an application of a coda modeling approach previously developed by Sens-Schönfelder and Wegler (2006) and later modified by Eulenfeld and Wegler (2016) and secondly the main focus of the current work is on the source parameter estimation. I also added an explanation about possible trade-offs (lines# 206-210).

Reviewer 2: In the studied area, I imagine that there are strong lateral variations of geology and therefore that the scattering coefficient depends on the source station pair. Is this taken into account in your inversion? If so, could you comment on the spatial variations of g in the studied area?

T.E: We appreciate reviewer for raising this point. The reviewer 2 is right about lateral heterogeneities in the study region. To consider this I specifically classified station-event pairs into two regional groups: those lying within Kırşehir Block and within Anatolide-

Tauride Block that are separated by the Central Anatolia Fault System. However, I should also notice that the approach used here does not require a priori knowledge of scattering and intrinsic attenuation. Resultant attenuation terms estimated following the simultaneous inversion procedure indicated an overall dominance of intrinsic attenuation over scattering one. A detailed discussion will be the out of our scope in the present study but certainly will be subject to future work that will be primarily focusing on crustal heterogeneities based on lateral variation of anelastic attenuation properties of the study region.

Reviewer 2: Is Figure 4 discussed somewhere in the text? I could not find. If the Figure is not useful, you should suppress it. If it contains information, please discuss it more carefully.

T.E.: This issue was earlier pointed out by reviewer 1 and it stems from a mistake when citing Figure 5. I already corrected this. Figure 4 is now also cited properly in the revised version of the text.

Reviewer 2: On L.250 and elsewhere, it is said that the radiation pattern has only a minor influence on the coda, an assertion with which I agree on the whole. Nevertheless, the separation of scattering and absorption also uses the energy contained the coherent wave which is strongly affected by the radiation pattern. If you have used techniques such as MLTWA in the past, you have probably observed that the largest fluctuations in the data occur in the window containing the ballistic wave. Therefore, it is not completely clear to me how the radiation pattern affects the data inversion. Could you comment on this point?

T.E.: The source radiation pattern is ignored in this assumption since averaging effect of multiple-scattering process ceases its effect on the S-wave coda. However it could be still influential on direct S wave portion in a way by altering attenuation estimates in cases of poor azimuthal coverage of station distribution with respect to earthquakes. In our case, the seismic network used in this study has relatively good azimuthal coverage, and thus direct S-wave measurements averaged over a lot of stations vanish influence of source radiation pattern on the attenuation estimates. The source radiation patterns, for example, will probably have a minor effect on our results because in the late coda the effect vanishes due to the averaging by multiple scattering and the direct S-wave is measured and averaged over a lot of stations.

1 **Moment magnitude estimates for Central Anatolian earthquakes using coda waves**

2 Tuna Eken¹

3

4 ¹*Department of Geophysical Engineering, the Faculty of Mines, Istanbul Technical*

5 *University, 34469 Maslak, Sariyer, Istanbul, Turkey*

6

7 *Abstract*

8 Proper estimate of moment magnitude that is a physical measure of the energy released at
9 earthquake source is essential for better seismic hazard assessments in tectonically active
10 regions. Here a coda wave modeling approach that enables the source displacement spectrum
11 modeling of examined event was used to estimate moment magnitude of central Anatolia
12 earthquakes. To achieve this aim, three component waveforms of local earthquakes with
13 magnitudes $2.0 \leq M_L \leq 5.2$ recorded at ~~72~~ 69 seismic stations which have been operated
14 between 2013 and 2015 within the framework of the CD-CAT passive seismic experiment
15 were utilized. An inversion on the coda wave traces of each selected single event in our
16 database was performed in five different frequency bands between 0.75 and 12 Hz. Our
17 resultant moment magnitudes (M_W -coda) exhibit a good agreement with routinely reported
18 local magnitude (M_L) estimates for the study area. Apparent move-out that is, particularly,
19 significant around the scattered variation of M_L - M_W -coda data points for small earthquakes
20 ($M_L < 3.5$) can be explained by possible biases of wrong assumptions to account for anelastic
21 attenuation and of seismic recordings with finite sampling interval. Finally, we present an
22 empirical relation between M_W -coda and M_L for central Anatolian earthquakes.

23

24 Keyword(s): Coda waves modelling, seismic moment, moment magnitude, Radiative Transfer

25 Theory

26 1. *Introduction*

27 The robust and stable knowledge of source properties (e.g. moment magnitude estimates) is
28 crucial in seismically active countries such as Turkey for a better evaluation of seismic hazard
29 potential as this highly depends on establishment of reliable seismicity catalogs. Moreover,
30 accurate information on source parameters could be important when developing regional
31 attenuation properties.

32

33 Conventional type of magnitude scales (M_L , m_b , M_S) as the result of empirically derived using
34 direct wave analyses can be biased due to various effects such as source radiation pattern,
35 directivity, and heterogeneities along the path since they may cause drastic changes in direct
36 wave amplitude measurements (e.g., Favreau and Archuleta, 2003). Instead several early
37 studies depending on the analysis of local and/or regional coda envelopes have indicated that
38 coda wave amplitudes are significantly less variable by a factor of 3-to-5 compared to direct
39 wave amplitudes (e.g., Mayeda and Walter, 1996; Mayeda et al., 2003; Eken et al., 2004;
40 Malagnini et al., 2004; Gök et al., 2016). In fact local or regional coda waves that are usually
41 considered to be generally ~~to be~~ composed of scattered waves. ~~and can~~ These wave trains ~~can~~
42 be simply explained by ~~that sample~~ the single scattering model of Aki (1969) ~~which~~ have
43 been proven to be virtually insensitive to any source radiation pattern effect in contrast to
44 direct waves ~~because of due to~~ the volume averaging property of the coda waves sampling the
45 entire focal sphere (e.g., Aki and Chouet, 1975; Rautian and Khalturin, 1978). In Sato and
46 Fehler (1998) and Sato et al. (2012) an extensive review study on the theoretical background
47 of coda generation and advances of empirical observations and modelling efforts can be found
48 in details.

49

50 There have been several approaches used for extracting information on earthquake source size
51 via coda wave analyses. These approaches can be mainly divided into two groups. The first
52 group of studies ~~can be considered as the parametric approach and essentially employs~~ coda
53 normalization strategy in which measurements require a correction for ~~empirically derived~~
54 ~~quality factors representing~~ seismic attenuation parameters (e.g. intrinsic and scattering) ~~that~~
55 ~~can be described by some empirical quality factors~~. In this case, ~~To calibrate the adjustment~~
56 ~~of~~-final source properties ~~are achieved with the help of some~~ reference events ~~whose seismic~~
57 ~~moments are previously estimated based on waveform inversion methods. are used to adjust~~
58 ~~measurements with respect to each other~~. For forward generation of synthetic coda envelopes,
59 either single-backscattering or more advanced multiple-backscattering approximation are
60 used. An example to this group is an empirical method originally developed by Mayeda et al.
61 (2003) to investigate seismic source parameters such as energy, moment, and apparent stress
62 drop in the western United States and in Middle East. They corrected observed coda
63 envelopes for various influences, for instance, path effect, S-to-coda transfer function, site
64 effect, and any distance-dependent changes in coda envelope shape. Empirical coda envelope
65 method have been successfully applied to different regions with complicated tectonics such as
66 northern Italy (e.g. Morasca et al., 2008), Turkey and Middle East (e.g. Eken et al., 2004; Gök
67 et al. 2016); or Korean Peninsula (e.g. Yoo et al., 2013).

68
69 Second type of approach ~~depends on estimating source and structural properties through a~~ is a
70 joint inversion technique. This technique employs ~~that is based on~~ a simultaneous
71 optimization of source, path, and site specific terms via a ~~fitting procedure between physically~~
72 ~~derived~~ synthetic ~~coda envelope~~ and observed coda envelope ~~fitting~~ within a selected time
73 window ~~including that includes both the~~ observed coda and direct-S wave parts. ~~Although the~~
74 ~~conventional coda-normalization method essentially relies on the correction for undesired~~

75 effects of the source and site amplifications, it may fail for small events with a shorter coda.
76 This mainly stems from random seismic noise that dominates the coda, which does not satisfy
77 the requirement of homogeneous distribution of energy in space. In the present study, we
78 avoid this shortcoming by involving source excitation and site amplification terms in the
79 inversion process. ~~In this approach,~~ To achieve this, the Radiative Transfer Theory (RTT) is
80 employed for analytic expression of synthetic coda wave envelopes. The method ~~that does not~~
81 ~~rely on coda normalization strategy~~ was originally developed by Sens-Schönfelder and
82 Wegler (2006) and successfully tested on local and regional earthquakes ($4 \leq M_l \leq 6$) detected
83 by the German Regional Seismic Network. Further it has been applied to investigate source
84 and frequency dependent attenuation properties of different geological settings, i.e., Upper
85 Rhine Graben and Molasse Basin regions in Germany and western Bohemia/Vogtland in
86 Czechia (Eulenfeld and Wegler, 2016); entire United States (2017); central and western
87 North Anatolian Fault Zone (Gaebler et al., 2018; Izgi et al., 2018). A more realistic earth
88 model in which anisotropic scattering conditions were earlier considered by Gusev and
89 Abubakirov (1987) yielded peak broadening effects of the direct seismic wave arrivals. This
90 approach ~~later was used in previous studies (e.g. Zeng, 1993; Przybilla and Korn, 2008;~~
91 ~~Gaebler et al., 2015)~~ that ~~examines dealt with the~~ propagation of P-wave elastic energy and
92 the effect of conversion between P- and S-wave energies was later used in Zeng and Aki
93 (1991) ~~1993, Przybilla and Korn (2008), Gaebler et al. (2015).~~

94
95 In the current work I present estimated source spectra as ~~an the~~ output of a joint inversion of
96 S- and coda waves parts ~~of~~ extracted from ~~local earthquake waveforms~~ 487 local earthquakes
97 with magnitudes $2.0 < M_l < 4.5$ detected in central Anatolia ~~for their source parameters~~. The
98 approach used here employs isotropic acoustic RTT approach for forward calculation of
99 synthetic coda envelopes. Gaebler et al. (2015) ~~have has~~ observed that modeling results from

100 isotropic scattering were almost comparable with those inferred from relatively more complex
101 elastic RTT simulations with anisotropic scattering conditions. The use of a joint inversion
102 technique is advantageous since it is insensitive to any potential bias, which could be
103 introduced by external information, i.e., source properties of a reference that is obtained
104 separately from other methods for calibration. This is mainly because of the fact that we
105 utilize an analytical expression of physical model involving source, and path related
106 parameters to describe the scattering process. Moreover the type of optimization during joint
107 inversion enables the estimates for source parameters of relatively small sized events
108 compared to the one used in coda-normalization methods.

109

110 2. *Regional Setting ~~and Data~~*

111 Present tectonic setting of Anatolia and surrounding regions have been mainly **the** outcome of
112 the northward converging movements among Africa, Arab, and Eurasian plates. To the west,
113 **the** subducting African plate with a slab roll-back dynamics beneath Anatolia along Hellenic
114 Trench has led to back-arc extension in the Aegean and western Anatolia, while
115 compressional deformation to the east around the Bitlis–Zagros suture was explained by
116 collisional tectonics (e.g. Taymaz et al., 1990; Bozkurt, 2001) (Fig. 1). Central Anatolia is
117 located between **an** extensional regime to the west due to the subduction, and **a** compressional
118 regime **tectonics** to the east due to the collisional tectonics. There are several fault systems
119 responsible for ongoing seismic activity in the region. The major fault zone, the Central
120 Anatolian Fault Zone (CAFZ) (Fig. 2), which primarily represents a transtensional fault
121 structure with **a** small amount of left-lateral offset during the Miocene (e.g. Koçyiğit and
122 Beyhan, 1998), can be considered as a boundary between the carbonate nappes of the
123 Anatolide-Tauride block ~~from~~ **and** the highly deformed and metamorphosed rocks in the
124 Kırşehir block. To the northwest of the CAFZ, Tuz Gölü Fault Zone (TGFZ) (Fig. 2), which

125 is characterized by a right-lateral strike slip motion with a significant oblique-slip normal
126 component, appears to be collocated with the Tuz Gölü Basin sedimentary deposits as well as
127 the crystalline rocks within the Kırşehir Block (e.g. Çemen et al., 1999; Bozkurt et al., 2001;
128 Taymaz et al., 2004; Çubuk et al., 2014). At the southwest tip of the study region, the EAFZ
129 generates large seismic activity that can be identified by rather complicated seismotectonic
130 setting: predominantly left-lateral strike-slip motion that is well correlated well with the
131 regional deformation pattern but also and with existing local clusters of thrust and normal
132 faulting events on NS- and EW-trending subsidiary faults, respectively (Bulut et al., 2012).
133 Such complicated behavior explains kinematic models (e.g. Riedel shear, anti-Riedel shear
134 models) of the shear deformation zone evolution (Tchalenko, 1970). It connects to the NAFZ
135 at the Karlıova Triple Junction (Bozkurt, 2001) and to the south splits into various segments
136 nearby the Adana Basin (Kaymakci et al., 2006) (Fig. 2). Toward the south, the EAFZ reaches
137 the Dead Sea Fault Zone (DSFZ) that has a key role in accommodating northward relative
138 motions of Arabian and African Plates with respect to Eurasia.

139

140 *3. Data*

141 The present work utilizes three-component waveforms of local seismic activity detected at 72
142 broadband seismic stations (Fig. 2) that have been operated for 2 years between 2013 and
143 2015 within the framework of a temporary passive seismic experiment, the Continental
144 Dynamics–Central Anatolian Tectonics (CD-CAT) (Portner et al., 2018). We benefit from
145 revisited standard earthquake catalogue information that is routinely released by the Kandilli
146 Observatory and Earthquake Research Institute (KOERI) (publicly available at
147 <http://www.koeri.boun.edu.tr>) to extract waveform data for a total of 2231 examined events
148 with station-event pair distance less than 120 km and focal depths less than 10 km. Most of
149 the detected seismic activity in the study area is associated to several fault zones in the region,

150 i.e., the EAFZ, CAFZ, DSFZ, TGFZ, etc. Here we note that ~~selection~~ the use of only local
151 earthquakes is to exclude possible biases, which may be introduced by Moho boundary
152 guided Sn-waves. ~~while~~ Upper crustal earthquakes ~~with less than 10 km focal depths~~ are
153 preferred in this study to exclude effect of relatively large-scale heterogeneities on coda wave
154 trains. ~~Finally~~ ~~Additionally~~, we ~~performed~~ a visual inspection ~~conducted~~ over all waveforms
155 to ensure high-quality waveforms. ~~and this reduces~~ Our final event number ~~reduced~~ to 1193.
156 Selected station and event distributions can be seen in Figure 2.

157

158 Observed waveforms were prepared at 5 different frequency bands with central frequencies at
159 0.75, 1.5, 3.0, 6.0, 12.0 Hz via a Butterworth band-pass filtering process. In the next step, we
160 applied Hilbert transform to filtered waveform data in order to obtain the total energy
161 envelopes. An average crustal velocity model was used to predict P and S wave onsets on
162 envelopes and then based on this information: (i) the noise level prior to the P-wave onset was
163 eliminated (ii) S-wave window was determined starting at 3s prior to and 7 s afterwards S-
164 wave onset as this allowed to include all direct S-wave energy, (iii) starting at the end of the
165 S-wave window, a coda window of 100s at maximum was determined. Length of coda
166 windows can be shorter when signal-to-noise ratio (SNR) is less than 2.5. ~~If there are or when~~
167 ~~the same window consists of there are~~ coda waves from two earthquakes (e.g. because of an
168 ~~aftershock sequence~~) within the same analysis window, which can ~~give rise to~~ can cause
169 ~~another rise instead of a decline in the envelope~~. We omit the earthquakes with less than 10 s
170 of coda length from our database. ~~Taking into account of these criteria, finally coda~~
171 ~~waveforms extracted from 6541 source-receiver pairs were used for further data process.~~

172

173

174

175 4. Method

176 We adopted an inversion procedure that was originally developed by Sens-Schönfelder and
 177 Wegler (2006) and later modified by Eulenfeld and Wegler (2016). The forward part, which
 178 involves calculation of energy density for a specific frequency band ~~caused by~~ under
 179 ~~assumption of~~ an isotropic source, is expressed in Sens-Schönfelder and Wegler (2006) as
 180 follows:

$$181 \quad E_{mod}(t, r) = WR(r)G(t, r, g)e^{-bt} \quad (1)$$

182
 183 where W gives source term and it is frequency dependent. $R(r)$ indicates the energy site
 184 amplification factor and b is intrinsic attenuation parameter. $G(t, r, g)$ represents Green's
 185 function that includes scattered wave field as well as direct wave and its expression is given
 186 by Paasschens (1997) as follows:

$$187 \quad G(t, r, g) = e^{(-v_0 t g_0)} \left[\frac{\delta(r - v_0 t)}{4\pi r^2} + \left(\frac{4\pi v_0}{3g_0} \right)^{-\frac{3}{2}} t^{-\frac{3}{2}} \times \left(1 - \frac{r^2}{v_0^2 t^2} \right)^{\frac{1}{8}} K \left(v_0 t g_0 \left(1 - \right. \right. \right. \\ 188 \left. \left. \left. \frac{r^2}{v_0^2 t^2} \right)^{\frac{3}{4}} \right) H(v_0 t - r) \right] \quad (2)$$

189 Here the term within Dirac delta function represents direct wave and other term indicates
 190 scattered waves. v_0 describes the mean S-wave velocity while g_0 is the scattering coefficient.

191 Possible discrepancy between predicted (Eq. 1) and observed energy densities for each event
 192 at each station with N_{ij} time samples (index k) in a specific frequency band can be minimized
 193 using:

$$194 \quad \epsilon(g) = \sum_{i,j,k}^{N_S, N_E, N_{ij}} (\ln E_{ijk}^{obs} - \ln E_{ijk}^{mod}(g))^2 \quad (3)$$

196

197 Here, the number of stations (index i) and events (index j) are shown by N_S and N_E ,
198 respectively. Optimization of g will be achieved by fulfilling following equalities:

199

$$200 \quad \ln E_{ijk}^{obs} = \ln E_{ijk}^{mod} \quad (4) \quad \text{or}$$

201

$$202 \quad \ln E_{ijk}^{obs} = \ln G(t_{ijk}, r_{ijk}, g) + \ln R_i + \ln W_j - bt_{ijk} \quad (5)$$

203 Equation 5 simply define an overdetermined inversion problem with $\sum_{i,j} N_{ij}$ number equation
204 systems and with $N_S + N_E + 1$ variables and thus b , R_i , and W_j can be solved via a least-
205 squares technique. $\epsilon(g)$ can be defined as sum over the squared residuals of the solution. As
206 can be seen from equation 1 that there is an obvious trade-off between R_i and W_j , which we
207 can manage by fixing the geometrical mean of R_i to 1 ($\Pi R_i = 1$). Equation 1 also implies
208 rather moderate trade-off between W_j and b . Trade-off between g and other inverted
209 parameters are usually small since this parameter is fixed through the energy ratio of the
210 direct S-wave and the level of the coda-waves (Gaebler et al., 2018).

211 Eulenfeld and Wegler (2016) present a simple recipe to perform the inversion:

212 (i) Calculate Green's functions through the analytic approximation of the solution for 3-D
213 isotropic radiative transfer (e.g. Paasschens 1997; Sens-Schönfelder and Wegler, 2006) by
214 using fixed scattering parameters and minimize equation 5 to solve for b , R_i , and W_j via a
215 weighted least-squares approach.

216 (ii) Calculate $\epsilon(g)$ using equation 3.

217 (iii) Repeat (i) and (ii) by selecting different g to find the optimal parameters g , b , R_i and W_j

218 that finally minimize the error function ϵ .

219 In Fig. 3 an example for the minimization process that was applied at five different frequency
220 bands is displayed for one selected event at recorded stations of the CD-CAT project.

221 Minimization described above for different frequencies will yield unknown spectral source
222 energy term, W_j as well as site response, R_i and attenuation parameters, b , and g that will
223 satisfy optimal fitting between observed and predicted coda wave envelopes. Example for this
224 fitting can be seen in Figure 4. The present study deals with frequency dependency of W_j
225 since this information can be later useful to obtain source displacement spectrum and thus
226 seismic moment and moment magnitudes of analyzed earthquakes using the formula of the S -
227 wave source displacement spectrum for a double-couple source in the far-field, which is given
228 by Sato et al. (2012):

$$229 \quad \omega M(f) = \sqrt{\frac{5\rho_0 v_0^5 W}{2\pi f^2}} \quad (6)$$

230 where W indicates the radiated S -wave energy at a center frequency f while v_0 and ρ_0
231 represent the mean S -wave speed and medium density, respectively.

232 The relation between the obtained source displacement spectrum and seismic moment value
233 was earlier described in Abercrombie (1995) by:

$$234 \quad \omega M(f) = M_0 \left(1 + \left(\frac{f}{f_c}\right)^n\right)^{-\frac{1}{\gamma}} \quad (7)$$

235 where n is related to the high-frequency fall-off and γ is known as shape parameter that
236 controls the sharpness of spectrum at corner frequency between the constant level M_0 (low
237 frequency part) and the fall-off with f^{-n} (high frequency part). Taking the logarithm of
238 equation 7 gives:

239

$$\ln \omega M(f) = \ln M_0 - \frac{1}{\gamma} \ln \left(1 + \left(\frac{f}{f_c} \right)^{\gamma c} \right) \quad (8)$$

241

242 ~~Eq. 8 describes an optimization problem and left hand side of the equation represents the data~~

243 ~~part that is simply observed source displacement spectrum and left hand side includes four~~

244 ~~source parameters, M_0 , γ , n , and f_c are the unknown model parameters that can be resolved in~~

245 ~~a simultaneous least-squares inversion of the equation 8. Eq. 8 describes an optimization~~

246 ~~problem where the observed source displacement spectrum data (left-hand side) can be~~

247 ~~inverted for four unknown source parameters, M_0 , γ , n , and f_c (right-hand side) in a~~

248 ~~simultaneous least-squares inversion scheme. Finally moment magnitude, M_w can be~~

249 ~~calculated from modeled source parameters, seismic moment, M_0 using a formula given by~~

250 ~~Hanks and Kanamori (1979):~~

251

$$M_w = \frac{2}{3} \log_{10} M_0 - 10.7 \quad (9)$$

253

254 *5. Results and Discussions*

255 *5.1 Coda wave source spectra*

256 Figure 5 displays observed values of source spectra established by inserting inverted spectral

257 source energy term W at each frequency in Eq. 6 for all analyzed events. Each curve in this

258 figure represents the model spectrum estimate based on the inversion procedure described in

259 the previous section. Modeled spectrum characteristics computed for 487 local earthquakes

260 whose geographical distribution of which lateral distribution is presented in Figure 2 suggest,

261 in general, that we were able to obtain typically expected source displacement spectrum with

262 a flat region around the low frequency limit and a decaying behaviour above a corner

263 frequency.

264

265 Owing to the multiple-scattering process within small scale heterogeneities that makes coda
266 waves gain an averaging nature, the variation in coda amplitudes due to differences in source
267 radiation pattern and path effect are reduced (Walter et al., 1995; Mayeda et al., 2003).
268 Eulenfeld and Wegler (2016) found that radiation pattern would have only a minor influence
269 on the S-wave coda while it might disturb attenuation models inferred from the direct S-wave
270 analyses unless the station distribution relative to the earthquakes indicates a good azimuthal
271 coverage. ~~A peak-like source function assumption for small earthquakes that are utilized in
272 the present work was earlier proven to be adequate in early application of the coda-wave
273 fitting studies (e.g. Sens-Schönfelder and Wegler, 2006; Gaebler et al., 2015; and Eulenfeld
274 and Wegler, 2016).~~

275

276 Conventional approaches (e.g. Abercrombie, 1995; Kwiatek et al., 2011) to estimate source
277 parameters such as corner frequency, seismic moment, high-frequency fall-off through fitting
278 of observed displacement spectra observed at a given station in an inversion scheme could be
279 misleading since these methods usually: (i) assume a constant value of attenuation effect (no
280 frequency variation) defined by a factor $\exp(-\pi ftQ^{-1})$ over the spectrum, (ii) and assume
281 omega-square model with a constant high-frequency fall-off parameter, $n=2$. Following Sens-
282 Schönfelder and Wegler (2006) and Eulenfeld and Wegler (2016), however, we estimate
283 attenuation parameters (intrinsic and scattering) separately within a simultaneous inversion
284 procedure in which high-frequency fall-off parameter varies. This is fairly consistent with
285 early studies (e.g. Ambeh and Fairhead, 1991; Eulenfeld and Wegler, 2016) where significant
286 deviations from the omega square model ($n>3$) were reported implying that the omega-square
287 model as a source model for small earthquakes must be reconsidered in its general
288 acceptance. Earlier it has been well-observed that the source spectra, especially, for large

289 earthquakes could be better explained by models of two corner frequencies (e.g.,
290 Papageorgiou and Aki, 1983; Joyner, 1984; Atkinson, 1990). Recently, Denolle et al. (2016)
291 observed that conventional spectral model of a single-corner frequency and high-frequency
292 fall-off rate could not explain P wave source spectra of thrust earthquakes with magnitude
293 M_w 5.5 and above. Instead, they suggested the double-corner-frequency model for large
294 global thrust earthquakes with a lower corner frequency related to source duration and with an
295 upper corner frequency suggesting a shorter time scale unrelated to source duration, which
296 exhibits its own scaling relation. Uchide and Imanishi (2016) reported similar differences
297 from the omega-square model would be valid also for smaller earthquakes by using spectral
298 ratio technique that involves empirical Green's function (EGF) events to avoid having a
299 complete knowledge of path and site effects for shallow target earthquakes (M_w 3.2–4.0) in
300 Japan. The source spectra for many of the target events in their study suggested a remarkable
301 discrepancy from the omega-square model for relatively small earthquakes. They explained
302 such differences by incoherent rupture due to heterogeneities in fault properties and applied
303 stress, the double-corner-frequency model, and possibility of a high-frequency falloff
304 exponent value slightly higher than 2. In our case, the smallest event was with M_w -coda
305 larger than 2.0, thus we had no chance to make a similar ~~comparison~~ compared to that of
306 Eulenfeld and Wegler (2016).; However, high-frequency fall-off parameters varied from
307 $n=0.5$ to $n=4$. A notable observation in the distribution of n was $n=2$ or $n=2.5$ would be better
308 explained for earthquakes with M_w -coda >4.0 whereas the smaller magnitudes exhibited more
309 scattered pattern of variation in n (Figure 7). Eulenfeld and Wegler (2016) claimed that the
310 use of separate estimates of the attenuation or correction for path effect via empirically
311 determined Green's function would be better strategy in order to invert station displacement
312 spectra for source parameters. This is mainly because smaller earthquakes (with $n>2$), in
313 particular, assuming omega-square model can distort the estimates of corner frequency and

314 even seismic moment especially in regions where Q is strongly frequency dependent. Thus,
315 independent estimates of Q during station displacement spectra inversions for source
316 parameters must be taken into account or the influence of path such as attenuation must be
317 removed via empirically determined Green's functions (Eulenfeld and Wegler, 2016).

318

319 *5.2 Coda wave –derived magnitude vs. M_L catalogue magnitude*

320 A scatter plot between catalogue magnitudes based on local magnitudes (M_L) and our coda-
321 derived magnitudes (M_W -coda) that are inferred from resultant frequency dependent source
322 displacement spectra and thus seismic moment (e.g. Eq. 9) is shown in Fig. 6. Such
323 comparison suggests an overall coherency between both types of magnitudes. This implies
324 that a very simple model of a first-order approximation for S-wave scattering with isotropic
325 acoustic radiative transfer approach can be efficient to link the amplitude and decaying
326 character of coda wave envelopes to the seismic moment of the source.

327

328 In the present study, a linear regression analyses performed between M_W -coda and M_L
329 magnitudes (Fig. 5) resulted in an empirical formula that can be employed to convert local
330 magnitudes into coda-derived moment magnitude calculation of local earthquakes in this
331 region:

332

$$333 \quad M_{W-coda} = 1.1655 \pm 0.0337 \times M_L - 0.7085 \pm 0.0128 \quad (10)$$

334

335 Bakun and Lindh (1977) empirically described the linear log seismic moment-local
336 magnitude relation between seismic moments (M_0) and local magnitudes (M_L) for
337 earthquakes near Oroville, California. Beside this several other studies investigated to find an
338 optimum relation between M_W and M_L by implementing linear and/or non-linear curve-fitting

339 approaches. Malagnini and Munafò (2018) proposed two different linear fits separated by a
340 crossover $M_L=4.31$ could represent M_L - M_W data points obtained from earthquakes of the
341 central and northern Apennines, Italy. Several coefficient of regression analyses in their fits
342 account for the combined effects of source scaling and crustal attenuation as well as regional
343 attenuation, focal depth, and rigidity at source. Goertz-Allmann et al. (2011), for instance,
344 introduced hybrid type of scaling relation that is linear below M_L 2 and above M_L 4 and a
345 quadratic relation in between ($2 \leq M_L \leq 4$) for earthquakes in Switzerland detected between
346 1998 and 2009. Edwards and Rietbrock (2009) employed a second-order polynomial equation
347 to relate local magnitudes routinely reported in the Japan Meteorological Agency (JMA)
348 magnitude and moment magnitude. More recently, using multiple spectral ratio analyses
349 Uchide and Imanishi (2018) estimated relative moment magnitudes for the Fukushima
350 Hamadori and the northern Ibaraki prefecture areas of Japan and reported a quadratic form of
351 correlation between JMA magnitudes and moment magnitudes. Resultant empirical curve in
352 Uchide and Imanishi (2018) implied a considerable discrepancy between the moment
353 magnitudes and the JMA magnitudes, with a slope of 1/2 for microearthquakes suggesting
354 possible biases introduced by anelastic attenuation and the recording by a finite sampling
355 interval.

356

357 Apparent move-out in Fig. 5 and Eq. 10, presumably stems from the use of different
358 magnitude scales for comparison. Conventional magnitudes scales such as M_L , mb inferred
359 from phase amplitude measurements are seemingly sensitive to attenuation and 2D variation
360 along the path (Pasyanos et al., 2016). Unlike local magnitude scales, seismic moment-based
361 moment magnitude (M_W) essentially represents a direct measure of the strength of an
362 earthquake caused by fault slip and is estimated from relatively flat portion of source spectra
363 at lower frequencies that can be less sensitive to the near surface attenuation effects. The

364 consistency between coda-derived moment magnitude and local magnitude scales for the
365 earthquakes with $M_{W-coda} > 3.0$ indicates that our non-empirical approach successfully
366 worked in this tectonically complex region. This observation is anticipated, for relatively
367 large earthquakes, since more energy will be characteristic at lower frequencies. We
368 observed similar type of consistency in early studies that investigate source properties of local
369 and regional earthquakes based on empirical coda methods with simple 1-D radially
370 symmetric path correction (e.g. Eken et al., 2004; Gök et al., 2016). Coda waves-derived
371 source parameters were obtained with high-precision in Mayeda et al. (2005), Phillips et al.
372 (2014), Pasyanos et al. (2016) following the use of 2-D path-corrected station techniques to
373 consider the amplitude-distance relationships. Observable outliers in Figure 5, for the events
374 with less than M_w 3.5, however, can be attributed to the either possible biases on local
375 magnitude values taken from the catalogue or small biases on our intrinsic (Q_i^{-1}) and
376 scattering (Q_s^{-1}) attenuation terms. One another possible contribution to such mismatch might
377 be associated to the influences of mode conversions between body and surface waves or
378 surface-to-surface wave scattering (~~e.g. Wu & Aki 1985~~) that are not restricted to low
379 frequencies (<1Hz) (Sens-Schönfelder and Wegler, 2006).

380

381 *6. Conclusions*

382 This study provides moment magnitude estimates as a direct physical measure of the seismic
383 energy for local earthquakes with magnitudes $2.0 \leq M_L \leq 5.2$ recorded at ~~72~~ 69 seismic
384 stations in central Anatolia. The source displacement spectra were obtained following the
385 application of a coda wave modeling procedure that employs a simultaneous optimization of
386 source, path, and site specific terms by fitting physically derived synthetic coda envelope and
387 observed coda envelopes. The Radiative Transfer Theory was used for analytic expression of
388 synthetic coda wave envelopes. Overall consistency between M_w -coda and M_L suggests that

389 our non-empirical approach successfully worked in this tectonically complex region.
390 Variation of high-frequency fall-off parameter indicated that for smaller earthquakes ($n > 2$)
391 assuming omega-square model can distort the estimates of corner frequency and even seismic
392 moment especially in regions where Q is strongly frequency dependent. Since the present
393 study mainly focuses on source properties of local earthquakes in the study area, scattering
394 and intrinsic attenuation properties that are other products of our coda envelope fitting
395 procedure will be examined in details within a future work. Finally, a linear regression
396 analyses resulted in an empirical relation developed between M_w -coda and M_L , which will be
397 a useful tool in the future to quickly convert catalogue magnitudes into moment magnitudes
398 for local earthquakes in the study area.

399

400 ~~This study provides an independent solution for estimating seismic source parameters such as~~
401 ~~seismic moment and moment magnitude for local earthquakes in central Anatolia without~~
402 ~~requiring *a priori* information on reference events with waveform modelling results to be~~
403 ~~used for calibration or *a priori* information on attenuation for path effect corrections. In this~~
404 ~~regard, the approach used here can be easy and useful tool for investigation of source~~
405 ~~properties of local events detected at temporal seismic networks. Moreover, seismic moment~~
406 ~~can be approximated via waveform modelling methods but due to the small scale~~
407 ~~heterogeneities of the media that waves propagate, it is often a hard task to establish Green's~~
408 ~~function for small earthquakes ($M_L < 3.5$). An analytical expression of energy density Green's~~
409 ~~function in a statistical manner employed in the present work enables neglecting the~~
410 ~~interaction of the small scale inhomogeneities with seismic waves as this can be practical for~~
411 ~~seismic moment calculations of small events that may pose source energy at high frequency.~~
412 ~~It is noteworthy to mention that our isotropic scattering assumption does not consider~~
413 ~~anisotropic case, which could be valid for real media, but still provides a simple and effective~~

414 ~~tool to define the transport for the anisotropic case since the estimated scattering coefficient~~
415 ~~can be interpreted as transport scattering coefficient. An averaging over S-wave window~~
416 ~~enables to overcome biases caused by using unrealistic Green's function (Gaebler *et al.*~~
417 ~~2015). Since the present study mainly focuses on source properties of local earthquakes in the~~
418 ~~study area, scattering and intrinsic attenuation properties that are other products of our coda~~
419 ~~envelope fitting procedure will be examined in details within a future work. Finally, the~~
420 ~~empirical relation developed between M_w -coda and M_L will be a useful tool for quickly~~
421 ~~converting catalogue magnitudes to moment magnitudes for local earthquakes in the study~~
422 ~~area.~~

423

424 *Data and resources*

425 The python code used for carrying out the inverse modeling is available under the permissive
426 MIT license and is distributed at <https://github.com/trichter/qopen>. We are grateful to the IRIS
427 Data Management Center for maintaining, archiving and making the continuous broadband
428 data used in this study open to the international scientific community. ~~The KOERI is specially~~
429 ~~thanked for providing publicly open local seismicity catalogues.~~

430

431 *Acknowledgement*

432 The facilities of IRIS Data Services, and specifically the IRIS Data Management Center, were
433 used for access to waveforms, related metadata, and/or derived products used in this study.
434 IRIS Data Services are funded through the Seismological Facilities for the Advancement of
435 Geoscience and EarthScope (SAGE) Proposal of the National Science Foundation under
436 Cooperative Agreement EAR-1261681. Data for the CD-CAT experiment
437 (https://doi.org/10.7914/SN/YB_2013) are available from the IRIS Data Management Center
438 at <http://www.iris.edu/hq/>. Tuna Eken acknowledge financial support from Alexander von

439 Humboldt Foundation (AvH) towards computational and peripherals resources. I am grateful
440 to the Topical Editor Charlotte Krawczyk for handling the revision process and Takahiko
441 Uchide and Ludovic Margerin for their valuable opinions on the improvement of manuscript.

442 *References*

443 Abercrombie, R.E.: Earthquake source scaling relationships from -1 to 5 ML using
444 seismograms recorded at 2.5-km depth, *J. geophys. Res.*, 100(B12), 24 015–24 036,
445 1995.

446 Aki, K., and Chouet., B.: Origin of coda waves: Source, attenuation, and scattering effects, *J.*
447 *Geophys. Res.* 80, 3322–3342, 1975.

448 Atkinson, G. M.: A comparison of eastern North American ground motion observations with
449 theoretical predictions, *Seismol. Res. Lett.* 61, 171–180, 1990.

450 Bakun, W.H. and Lindh, A.G.: Local Magnitudes, Seismic Moments, and Coda Durations for
451 Earthquakes Near Oroville, California, *Bulletin of the*
452 *Seismological Society of America*. Vol.67, No.3, pp. 615-629, 1977.

453 Bozkurt, E.: Neotectonics of Turkey—A synthesis: *Geodinamica Acta*, v. 14, p. 3–30, 2001.

454 Bulut, F., Bohnhoff, M., Eken, T., Janssen, C., Kılıç, T., and Dresen, G.: The East Anatolian
455 fault zone: Seismotectonic setting and spatiotemporal characteristics of seismicity based
456 on precise earthquake locations: *Journal of Geophysical Research*, v. 117, B07304,
457 <https://doi.org/10.1029/2011JB008966>, 2012.

458 Çemen, I., Göncüoğlu, M.C., and Dirik, K.: Structural evolution of the Tuz Gölü basin in central
459 Anatolia, Turkey: *Journal of Geology*, v. 107, p. 693–706, <https://doi.org/10.1086/314379>, 1999.

461 Çubuk Y, Yolsal-Çevikbilen S, Taymaz, T.: Source parameters of the 20052008 Bal[^]aSirapinar
462 (central Turkey) earthquakes: Implications for the internal deformation of the Anatolian
463 plate. *Tectonophysics* 635(Supplement C) :125 – 153, 2014.

464 Denolle, M. A., and Shearer, P.M.: New perspectives on self-similarity for shallow thrust
465 earthquakes, *J. Geophys. Res. Solid Earth*, 121, 6533–6565, 2016.

466 Edwards, B., & Rietbrock, A.: A comparative study on attenuation and source-scaling relations
467 in the Kantō, Tokai, and Chubu regions of Japan, using data from Hi-net and KiK-net.
468 *Bulletin of the Seismological Society of America*, 99, 2435–2460, 2009.

469 Eken, T., Mayeda, K., Hofstetter, A., Gök, R., Orgülü, G. and Turkelli, N.: An application of the
470 coda methodology for moment-rate spectra using broadband stations in Turkey.
471 *Geophys. Res. Lett.*, 31, L11609, 2004.

472 Eulenfeld, T. and Wegler, U.: Measurement of intrinsic and scattering attenuation of shear
473 waves in two sedimentary basins and comparison to crystalline sites in Germany,
474 *Geophys J Int.*, 205(2):744-757, 2016.

475 Eulenfeld, T. and Wegler, U.: Crustal intrinsic and scattering attenuation of high-frequency
476 shear waves in the contiguous United States. *J Geophys., Res*, 122, 2017.

477 Favreau, P., and Archuleta, R.J.: Direct seismic energy modelling and application to the 1979
478 Imperial Valley earthquake, *Geophys. Res. Lett.*, 30, 1198, 2003.

479 Gaebler, P.J., Eulenfeld, T. & Wegler, U.: Seismic scattering and absorption parameters in the
480 W-Bohemia/Vogtland region from elastic and acoustic radiative transfer theory,
481 *Geophys. J. Int.*, 203(3), 1471–1481, 2015.

482 Gaebler, P.J., Eken, T., Bektaş, H.Ö, Eulenfeld, T., Wegler, U., Taymaz, T.: Imaging of Shear
483 Wave Attenuation Along the Central Part of the North Anatolian Fault Zone, Turkey,
484 submitted to the *Journal of Seismology*, 2018.

485 Goertz-Allmann, B. P., Edwards, B., Bethmann, F., Deichmann, N., Clinton, J., Fäh, D., &
486 Giardini, D.: A new empirical magnitude scaling relation for Switzerland. *Bulletin of the*
487 *Seismological Society of America*, 101, 3088–3095, 2011.

488 Gök, R., Kaviani, A., Matzel, E. M., Pasyanos, M. E., Mayeda, K., Yetirmishli, G., El-Hussain,
489 I., Al-Amri, A., Al-Jeri, F., Godoladze, T., Kalafat, D., Sandvol, E. A., and Walter,
490 W.R.: Moment Magnitudes of Local/Regional Events from 1D Coda Calibrations in the
491 Broader Middle East Region. *Bull Seismol Soc Am.*, 106(5):1926-1938, 2016.

492 Gusev, A.A. & Abubakirov, I.R.: Simulated envelopes of non-isotropically scattered body
493 waves as compared to observed ones: another manifestation of fractal heterogeneity,
494 *Geophys. J. Int.*, 127(1), 49–60, 1996.

495 Hanks, T.C. and Kanamori, H.: A moment magnitude scale, *J. Geophys., Res.*, 84, 2348–2350,
496 1979.

497 Izgi, G., Eken, T., Gaebler, P., and Taymaz, T.: Frequency-Dependent Shear Wave Attenuation
498 Along the Western Part of the North Anatolian Fault Zone, *Geophysical Research*
499 *Abstracts*, Vol. 20, EGU2018-629-2, 2018.

500 Kaymakci, N. Inceöz, M. Ertepinar, P.: 3D architecture and Neogene evolution of the Malatya
501 Basin: inferences for the kinematics of the Malatya and Ovacik Fault Zones. *Turkish*
502 *Journal of Earth Sciences*, 15, 123-154, 2006.

503 Kwiatek, G., Plenkers, K. & Dresen, G.: 2011. Source parameters of pico-seismicity recorded at
504 Mponeng Deep Gold Mine, South Africa: implications for scaling relations, *Bull. seism.*
505 *Soc. Am.*, 101(6), 2592–2608, 2011.

506 Malagnini, L., Mayeda, K., Akinci, A., and Bragato, P. L.: Estimating absolute site effects,
507 *Bull. Seismol. Soc. Am.* 94, no. 4, 1343–1352, 2004.

508 Malagnini, L., and Munafò, I.: On the Relationship between M_L and M_w in a Broad Range: An
509 Example from the Apennines, Italy, *Bulletin of the Seismological Society of America*,
510 Vol. 108, No. 2, pp. 1018–1024, 2018.

511 Mayeda, K., and Walter, W.R.: Moment, energy, stress drop, and source spectra of western
512 United States earthquakes from regional coda envelopes, *J. Geophys. Res.* 101, 11,195–
513 11,208, 1996.

514 Mayeda, K., Hofstetter, A., O’Boyle, J.L., and Walter, W.R.: Stable and transportable regional
515 magnitudes based on coda-derived moment-rate spectra, *Bull. Seismol. Soc. Am.* 93,
516 224–239: 2003.

517 Mayeda, K., Malagnini, L., Phillips, W. S., Walter, W. R., and Dreger, D.: 2D or not 2D, that is
518 the question: A Northern California Test. *Geophysical Research Letters*, 32(12), 2005.

519 Morasca, P., Mayeda, K., Malagnini, L. and Walter, W.R.: Coda and direct-wave attenuation
520 tomography in northern Italy, *Bull Seismol Soc Am.*, v. 98, pages, 1936-1946, 2004.

521 Morasca, P., Mayeda, K., Gök, R., Phillips, W.S., and Malagnini, L.: Coda-derived source
522 spectra, moment magnitudes and energy-moment scaling in the western Alps, *Geophys.*
523 *J. Int.*, 160, 263–275, 2008.

524 Paasschens, J.: Solution of the time-dependent Boltzmann equation, *Phys. Rev. E*, 56(1), 1135–
525 1141, 1997.

526 Papageorgiou, A., and Aki, K.: A specific barrier model for the quantitative description of
527 inhomogeneous faulting and the prediction of strong ground motion I: Description of the
528 model, *Bull. Seismol. Soc. Am.*, 73(3), 693–722, 1983.

529 Pasyanos, M. E., R. Gök, and Walter, W.R.: 2-D variations in coda amplitudes in the Middle
530 East. *Bull. Seismol. Soc. Am.* 106, no. 5, 2016.

531 Phillips, W. S., Mayeda, K. M., and Malagnini, L.: How to invert multi-band, regional phase
532 amplitudes for 2-d attenuation and source parameters: Tests using the usarray. *Pure and*
533 *Applied Geophysics*, 171(3):469-484, 2014.

534 Portner, D.E., Delph, J.R., Biryol, C.B., Beck, S.L., Zandt, G., Özacar, A.A., Sandvol, E., and
535 Türkelli, N.: Subduction termination through progressive slab deformation across
536 Eastern Mediterranean subduction zones from updated P-wave tomography beneath
537 Anatolia, *Geosphere*, 14(3): 907-925, 2018.

538 Przybilla, J. and Korn, M.: Monte Carlo simulation of radiative energy transfer in continuous
539 elastic random mediathree-component envelopes and numerical validation. *Geophys J*
540 *Int* , 173(2):566-576, 2008.

541 Rautian, T.G. & Khalturin, V.I.: The use of the coda for determination of the earthquake source
542 spectrum, *Bull. Seism. Soc. Am.*, 68(4), 923–948, 1978.

543 Sato, H. and Fehler, M.C.: *Seismic Wave Propagation and Scattering in the Heterogeneous*
544 *Earth*, Springer-Verlag, New York, 1998.

545 Sato, H., Fehler, M.C. & Maeda, T. *Seismic Wave Propagation, and Scattering in the*
546 *Heterogeneous Earth*, 2nd edn, Springer: 2012.

547 Sens-Schönfelder, C. and Wegler, U.: Radiative transfer theory for estimation of the seismic
548 moment. *Geophys J Int*, 167(3):1363-1372.

549 Taymaz, T., Jackson, J., Westaway, R.: Earthquake mechanisms in the Hellenic Trench near
550 Crete. *Geophys. J. Int.*102, 695–731, 1990.

551 Taymaz, T., Westaway, R., Reilinger, R.: Active faulting and crustal deformation in the eastern
552 Mediterranean Region. *Spec. Issue Tectonophys.* 391 (1-4), 1–9. [http://](http://dx.doi.org/10.1016/j.tecto.2004.07.005)
553 dx.doi.org/10.1016/j.tecto.2004.07.005, 2004.

554 Tchalenko, J. S.: *Similarities between shear zones of different magnitudes. Geol. Soc. Am.*
555 *Bull.*, 81, 1625–1640, 1970.

556 Uchide, T., & Imanishi, K.: Small earthquakes deviate from the omega-square model as revealed
557 by multiple spectral ratio analysis. *Bulletin of the Seismological Society of America*,
558 106(3), 1357–1363, 2016.

559 Uchide, T., & Imanishi, K.: Underestimation of microearthquake size by the magnitude scale of
560 the Japan Meteorological Agency: Influence on earthquake statistics. *Journal of*
561 *Geophysical Research: Solid Earth*, 123, 606–620, 2018.

562 Yoo, S.-H., Rhie, J., Choi, H.-S., and Mayeda, K.: Coda-derived source parameters of
563 earthquakes and their scaling relationships in the Korean Peninsula, *Bull. Seismol. Soc.*
564 *Am.*, 101, 2388–2398, 2011.

565 ~~Wu, R. and Aki, K.: The fractal nature of the inhomogeneities in the lithosphere evidenced from~~
566 ~~seismic wave scattering, *Pure appl. Geophys.*, 123(6), 805–818, 1985.~~

567 Zeng, Y., Su, F. and Aki, K.: Scattering wave energy propagation in a random isotropic
568 scattering medium: 1. Theory, *J. Geophys. Res.*, 96(B1), 607–619, 1991.

569

570 *Figure Captions*

571 Figure 1. Major tectonic features of Turkey and its adjacent. The plate boundary data used
572 here is taken from Bird (2003). Subduction zones are black, continental transform faults are
573 red, continental rift boundaries are green, and spreading ridges boundaries are yellow. NAFZ,
574 EAFZ, and DSFZ are the North Anatolian Fault, East Anatolian Fault, and the Dead Sea fault,
575 respectively.

576

577 Figure 2. Epicentral distribution of all local events selected from the study area in the KOERI
578 catalogue. Gray circles represent earthquakes with poor quality that are not considered for the
579 current study while black indicates the location of local events with good quality. Red circles
580 among these events are 487 events used in coda wave inversion since they are successful at
581 passing quality criteria of further pre-processing procedure.

582

583 Figure 3. An example from the inversion procedure explained in chapter 3. Here coda
584 envelope fitting optimization is performed on band-pass filtered (4-8Hz-16Hz) digital
585 recordings of an earthquake (2014 April 09, M_w -coda3.2) extracted for 7 seismic stations that
586 operated within the CD-CAT array. Large panel at the lower left-hand side displays the error
587 function ε as a function of g_0 . Thick blue cross here represent the optimal value of $g = g_0$.
588 Other small panels at upper and right-hand side show the least- squares solution of the
589 weighted linear equation system for the first 6 guesses and optimal guess for g_0 . ~~There~~ The
590 dots and gray curves indicate the ratio between energy (E^{obs}) and the Green's function (G)
591 obtained for direct S-waves and observed envelopes at various stations, respectively (Please
592 notice that during this optimization process envelopes are corrected for the obtained site
593 corrections R_i). The slope of linear curve at each small panel yields $-b$ in relation to the
594 ~~intrinsic attenuation. The linear curve~~ has an intercept of W representing source related terms
595 at the right-hand side of equation 5 ~~part of the right-hand side of the equation system.~~

596

597 Figure 4. a) Results of the inversion of the 2014-April-09, M_w -coda3.2 earthquake: Sample
598 fits between observed and calculated energy densities in the frequency band 0.5–1.0 Hz are
599 given for 6 different stations (see upper right corner for event ID, station name, and distance
600 to hypocenter). Note that light blue curves represent observed envelope. Smoothed observed
601 calculated envelopes in each panel are presented by blue and red curves, respectively. Blue
602 and red dots exhibit location of the average value for observed and calculated envelopes
603 within the S-wave window, respectively. b) The same as in (a) obtained in the frequency band
604 4.0–8.0 Hz.

605

606 Figure 5. All individual observed (black squares) and predicted (gray curve) source
607 displacement spectra observed at 72 stations from 487 local earthquakes in central Anatolia.

608

609 Figure 6: Scatter plot between local magnitudes (M_L) of analyzed events with coda waves-
610 derived magnitudes (M_W -coda) of the same events. The outcome of a linear regression
611 analysis yielded an empirical formula (e.g. Eq. 10) to identify the overall agreement
612 represented by gray straight line. Yellow and red dashed lines indicate upper and lower limit
613 of linearly fitting to that scatter.

614

615 Figure 7: Same scatter plot displayed in Fig. 6. Here color coded ~~d~~ indicates ~~by~~ estimated high-
616 frequency fall-off parameter for each inverted event.

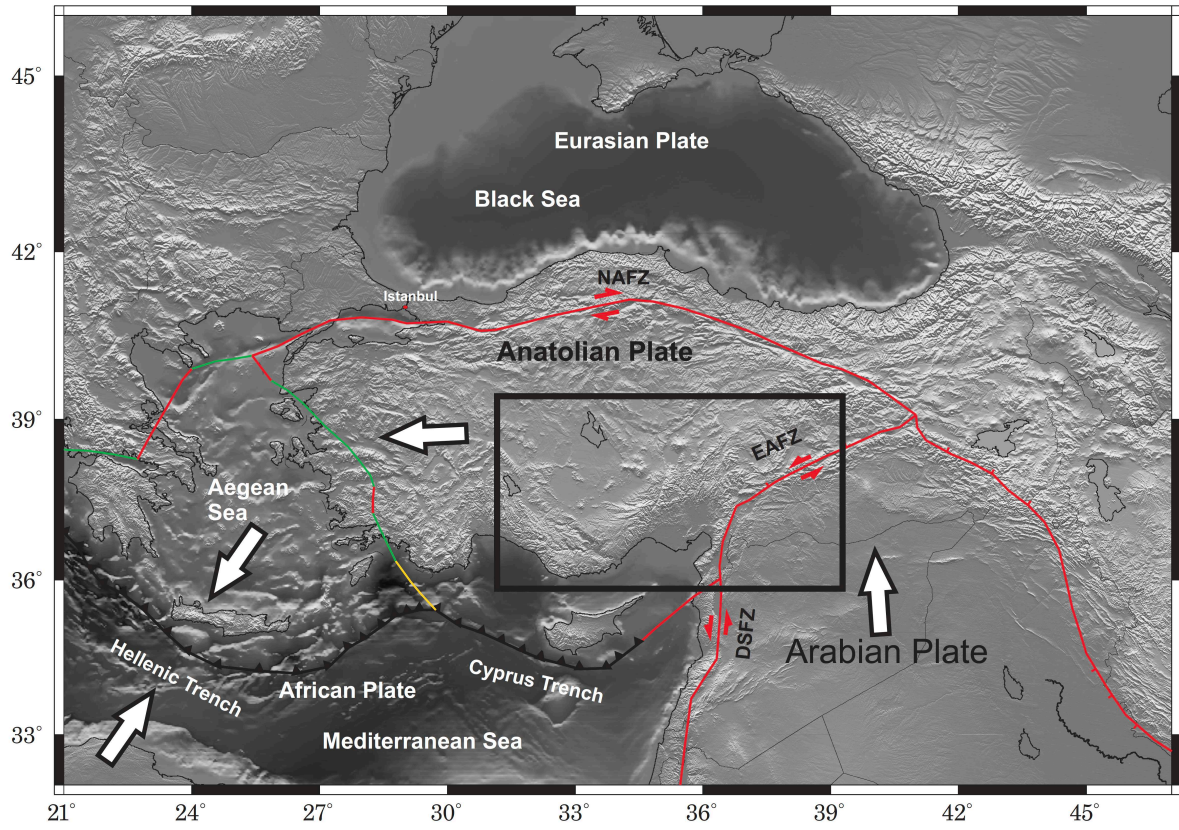
617

618

619

620

621



622

623

624

625 Figure 1.

626

627

628

629

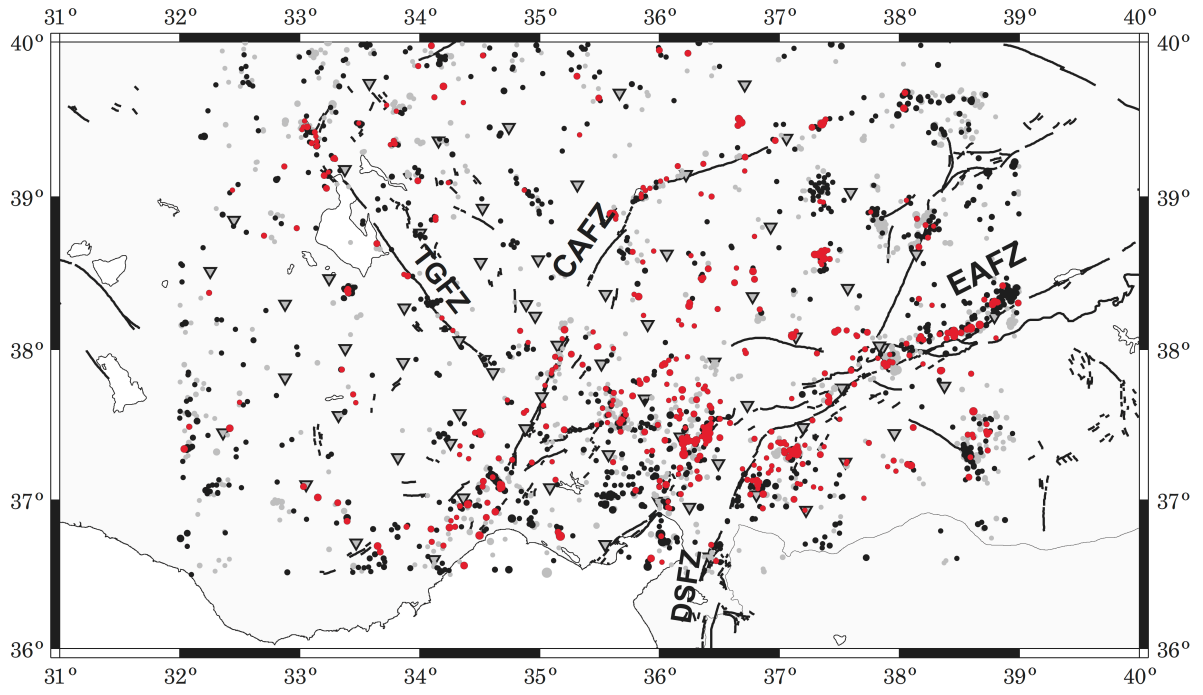
630

631

632

633

634



635

636 Figure 2.

637

638

639

640

641

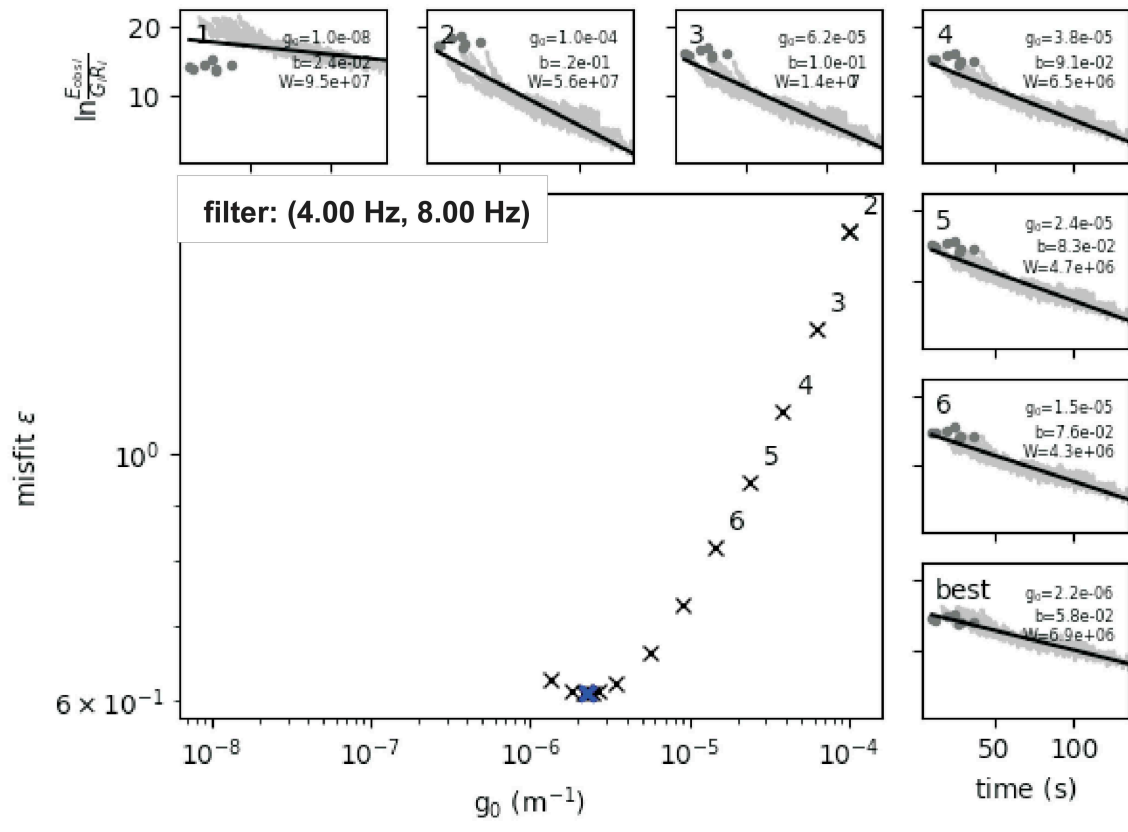
642

643

644

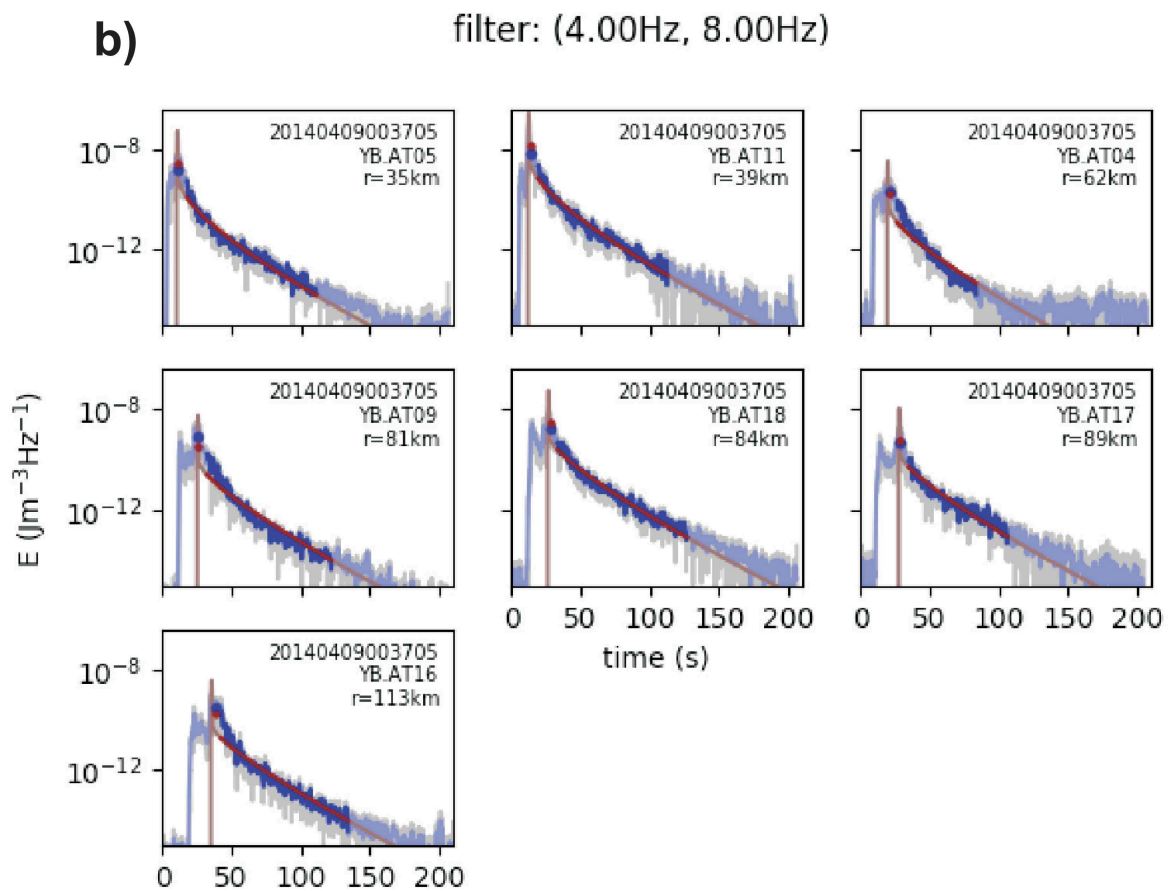
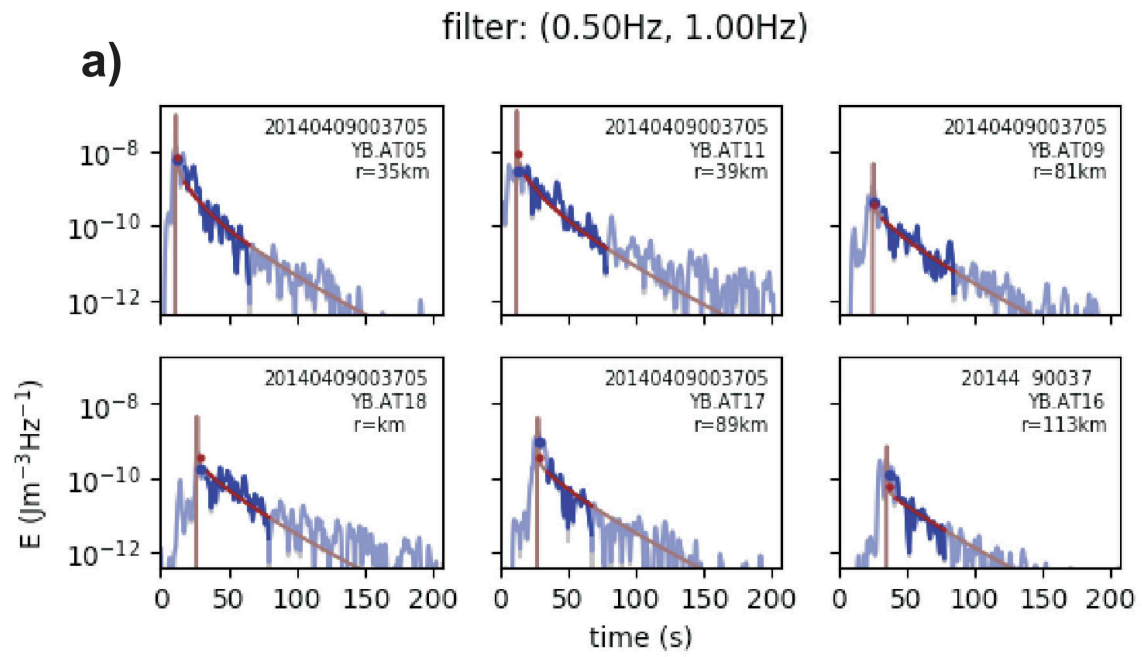
645

646



647
 648
 649
 650
 651

Figure 3.



652

653

654

655

656

657

658

Figure 4.

659
660
661
662
663

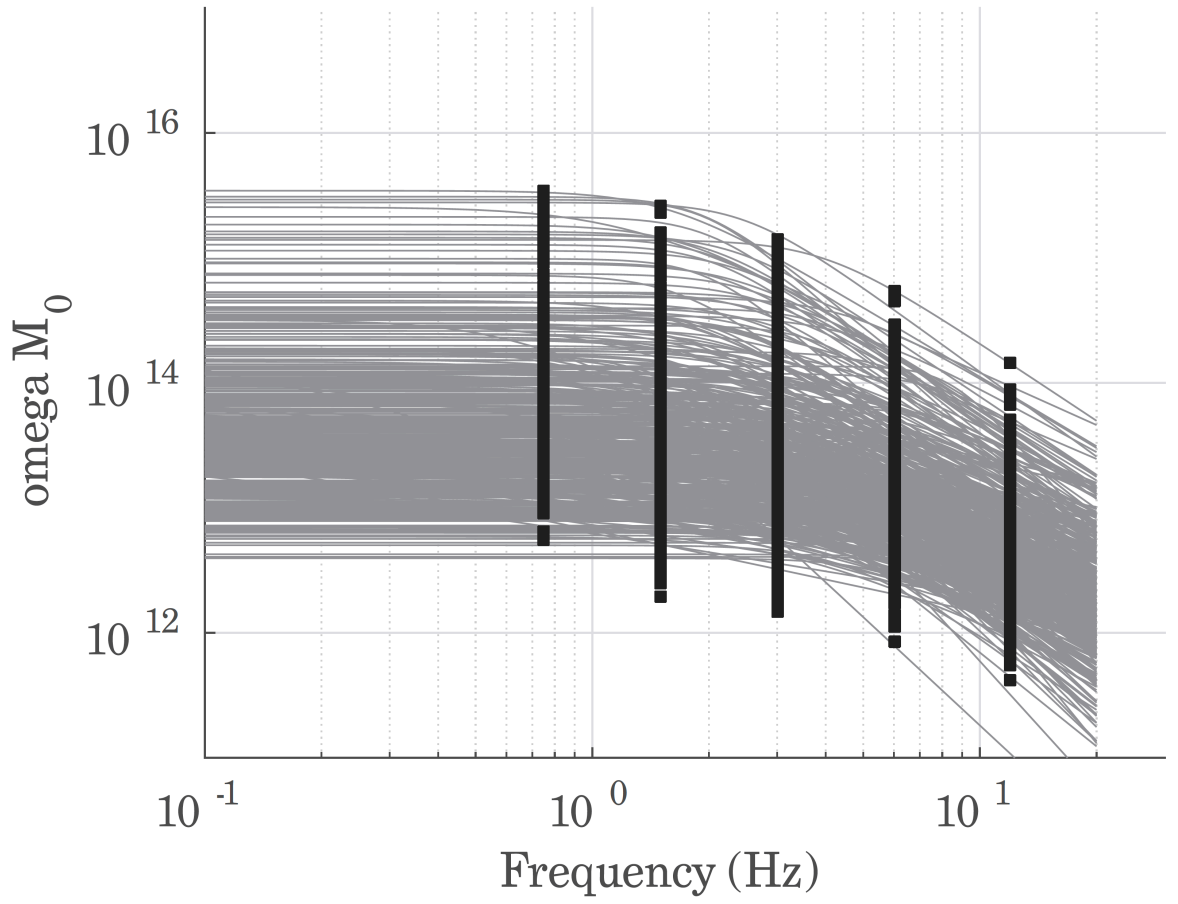


Figure 5.

664
665
666
667
668
669
670
671
672
673
674
675
676
677
678
679
680
681
682
683
684

685
686
687
688
689
690

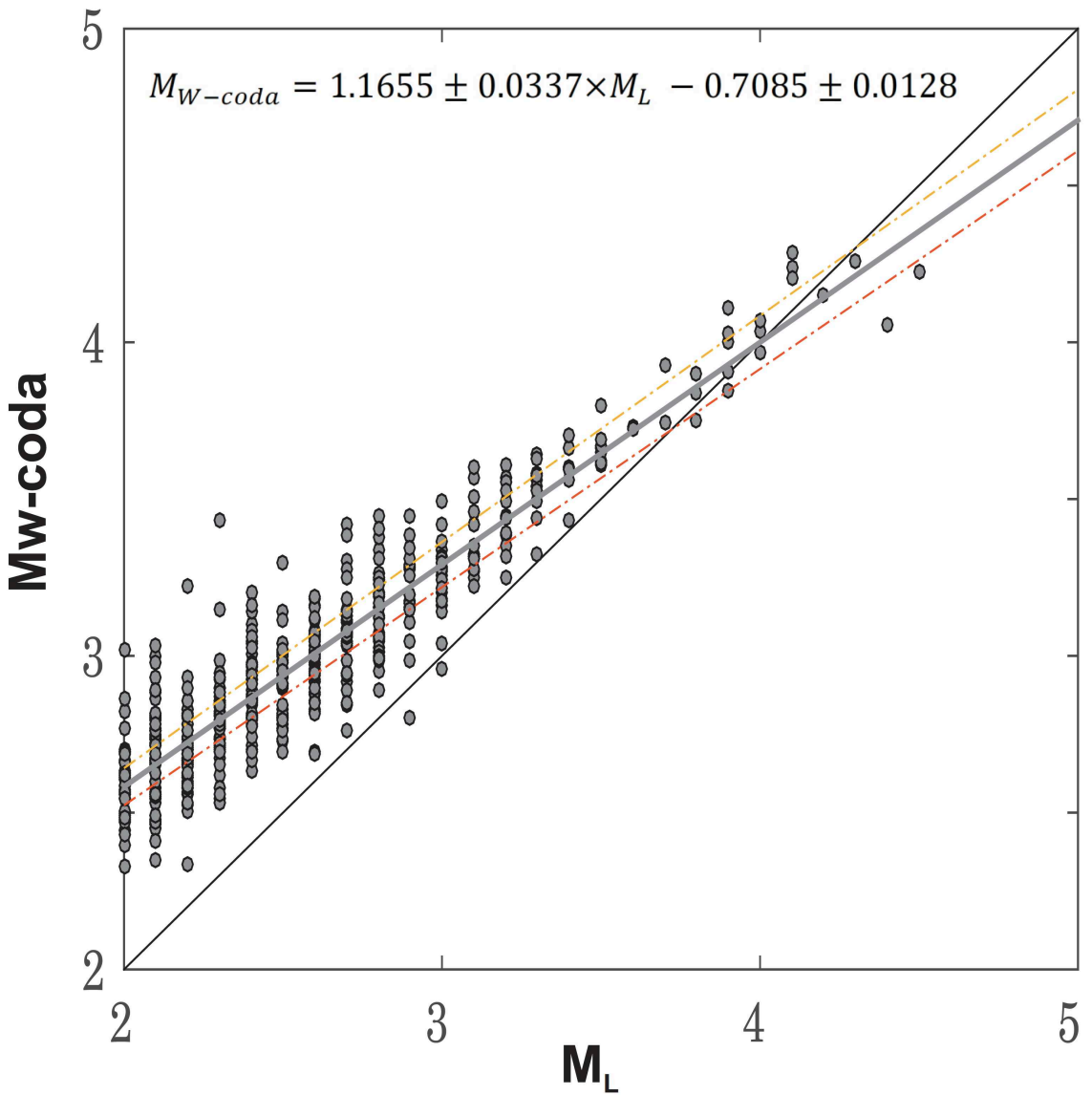
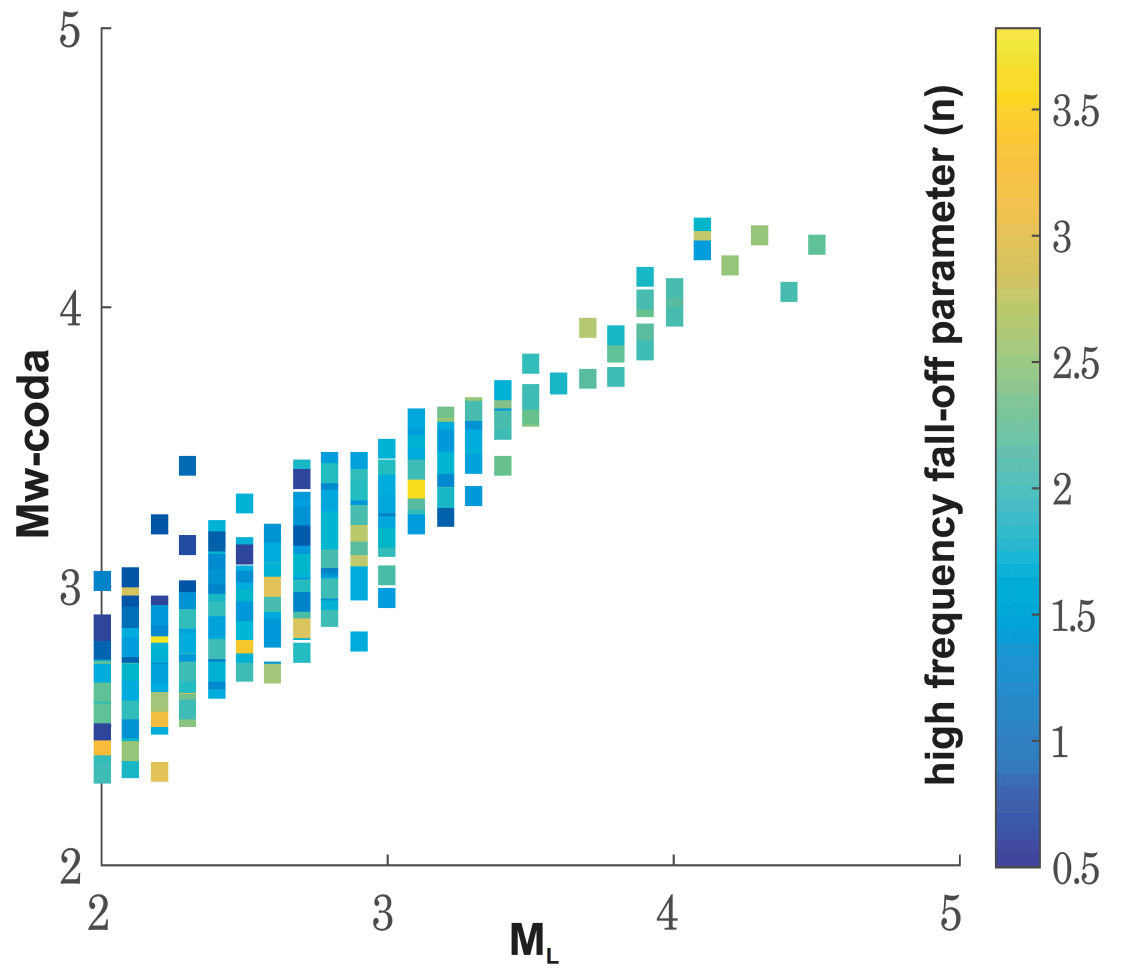


Figure 6.

691
692
693
694
695
696
697
698
699
700
701
702
703
704

705
706



707
708
709
710

Figure 7.

1 **Moment magnitude estimates for Central Anatolian earthquakes using coda waves**

2 Tuna Eken¹

3

4 ¹*Department of Geophysical Engineering, the Faculty of Mines, Istanbul Technical*

5 *University, 34469 Maslak, Sariyer, Istanbul, Turkey*

6

7 *Abstract*

8 Proper estimate of moment magnitude that is a physical measure of the energy released at
9 earthquake source is essential for better seismic hazard assessments in tectonically active
10 regions. Here a coda wave modeling approach that enables the source displacement spectrum
11 modeling of examined event was used to estimate moment magnitude of central Anatolia
12 earthquakes. To achieve this aim, three component waveforms of local earthquakes with
13 magnitudes $2.0 \leq M_L \leq 5.2$ recorded at 69 seismic stations which have been operated
14 between 2013 and 2015 within the framework of the CD-CAT passive seismic experiment
15 were utilized. An inversion on the coda wave traces of each selected single event in our
16 database was performed in five different frequency bands between 0.75 and 12 Hz. Our
17 resultant moment magnitudes (M_W -coda) exhibit a good agreement with routinely reported
18 local magnitude (M_L) estimates for the study area. Apparent move-out that is, particularly,
19 significant around the scattered variation of M_L - M_W -coda data points for small earthquakes
20 ($M_L < 3.5$) can be explained by possible biases of wrong assumptions to account for anelastic
21 attenuation and of seismic recordings with finite sampling interval. Finally, we present an
22 empirical relation between M_W -coda and M_L for central Anatolian earthquakes.

23

24 Keyword(s): Coda waves modelling, seismic moment, moment magnitude, Radiative Transfer

25 Theory

26 1. *Introduction*

27 The robust and stable knowledge of source properties (e.g. moment magnitude estimates) is
28 crucial in seismically active countries such as Turkey for a better evaluation of seismic hazard
29 potential as this highly depends on establishment of reliable seismicity catalogs. Moreover,
30 accurate information on source parameters could be important when developing regional
31 attenuation properties.

32

33 Conventional type of magnitude scales (M_L , m_b , M_S) as the result of empirically derived using
34 direct wave analyses can be biased due to various effects such as source radiation pattern,
35 directivity, and heterogeneities along the path since they may cause drastic changes in direct
36 wave amplitude measurements (e.g., Favreau and Archuleta, 2003). Instead several early
37 studies depending on the analysis of local and/or regional coda envelopes have indicated that
38 coda wave amplitudes are significantly less variable by a factor of 3-to-5 compared to direct
39 wave amplitudes (e.g., Mayeda and Walter, 1996; Mayeda et al., 2003; Eken et al., 2004;
40 Malagnini et al., 2004; Gök et al., 2016). In fact local or regional coda waves that are usually
41 considered to be generally composed of scattered waves. These wave trains can be simply
42 explained by the single scattering model of Aki (1969) which have been proven to be
43 virtually insensitive to any source radiation pattern effect in contrast to direct waves due to
44 the volume averaging property of the coda waves sampling the entire focal sphere (e.g., Aki
45 and Chouet, 1975; Rautian and Khalturin, 1978). In Sato and Fehler (1998) and Sato et al.
46 (2012) an extensive review study on the theoretical background of coda generation and
47 advances of empirical observations and modelling efforts can be found in details.

48

49 There have been several approaches used for extracting information on earthquake source size
50 via coda wave analyses. These approaches can be mainly divided into two groups. The first

51 group of studies can be considered as the parametric approach and essentially employs coda
52 normalization strategy in which measurements require a correction for empirically derived
53 quality factors representing seismic attenuation parameters (e.g. intrinsic and scattering). In
54 this case, adjustment of final source properties are achieved with the help of some reference
55 events whose seismic moments are previously estimated based on waveform inversion
56 methods. For forward generation of synthetic coda envelopes, either single-backscattering or
57 more advanced multiple-backscattering approximation are used. An example to this group is
58 an empirical method originally developed by Mayeda et al. (2003) to investigate seismic
59 source parameters such as energy, moment, and apparent stress drop in the western United
60 States and in Middle East. They corrected observed coda envelopes for various influences, for
61 instance, path effect, S-to-coda transfer function, site effect, and any distance-dependent
62 changes in coda envelope shape. Empirical coda envelope method have been successfully
63 applied to different regions with complicated tectonics such as northern Italy (e.g. Morasca et
64 al., 2008), Turkey and Middle East (e.g. Eken et al., 2004; Gök et al. 2016); or Korean
65 Peninsula (e.g. Yoo et al., 2013).

66
67 Second type of approach depends on estimating source and structural properties through a
68 joint inversion technique. This technique employs a simultaneous optimization of source,
69 path, and site specific terms via a fitting procedure between physically derived synthetic coda
70 envelope and observed coda envelope within a selected time window that includes both the
71 observed coda and direct-S wave parts. Although the conventional coda-normalization
72 method essentially relies on the correction for undesired effects of the source and site
73 amplifications, it may fail for small events with a shorter coda. This mainly stems from
74 random seismic noise that dominates the coda, which does not satisfy the requirement of
75 homogeneous distribution of energy in space. In the present study, we avoid this shortcoming

76 by involving source excitation and site amplification terms in the inversion process. To
77 achieve this, the Radiative Transfer Theory (RTT) is employed for analytic expression of
78 synthetic coda wave envelopes. The method was originally developed by Sens-Schönfelder
79 and Wegler (2006) and successfully tested on local and regional earthquakes ($4 \leq M_L \leq 6$)
80 detected by the German Regional Seismic Network. Further it has been applied to investigate
81 source and frequency dependent attenuation properties of different geological settings, i.e.,
82 Upper Rhine Graben and Molasse Basin regions in Germany and western Bohemia/Vogtland
83 in Czechia (Eulenfeld and Wegler, 2016); entire United States (2017); central and western
84 North Anatolian Fault Zone (Gaebler et al., 2018; Izgi et al., 2018). A more realistic earth
85 model in which anisotropic scattering conditions were earlier considered by Gusev and
86 Abubakirov (1987) yielded peak broadening effects of the direct seismic wave arrivals. This
87 approach that examines the propagation of P-wave elastic energy and the effect of conversion
88 between P- and S-wave energies was later used in Zeng and Aki (1991), Przybilla and Korn
89 (2008), Gaebler et al. (2015).

90

91 In the current work I present source spectra as the output of a joint inversion of S- and coda
92 waves parts extracted from 487 local earthquakes with magnitudes $2.0 < M_L < 4.5$ detected in
93 central Anatolia. The approach used here employs isotropic acoustic RTT approach for
94 forward calculation of synthetic coda envelopes. Gaebler et al. (2015) have observed that
95 modeling results from isotropic scattering were almost comparable with those inferred from
96 relatively more complex elastic RTT simulations with anisotropic scattering conditions. The
97 use of a joint inversion technique is advantageous since it is insensitive to any potential bias,
98 which could be introduced by external information, i.e., source properties of a reference that
99 is obtained separately from other methods for calibration. This is mainly because of the fact
100 that we utilize an analytical expression of physical model involving source, and path related

101 parameters to describe the scattering process. Moreover the type of optimization during joint
102 inversion enables the estimates for source parameters of relatively small sized events
103 compared to the one used in coda-normalization methods.

104

105 *2. Regional Setting*

106 Present tectonic setting of Anatolia and surrounding regions have been mainly the outcome of
107 the northward converging movements among Africa, Arab, and Eurasian plates. To the west,
108 the subducting African plate with a slab roll-back dynamics beneath Anatolia along Hellenic
109 Trench has led to back-arc extension in the Aegean and western Anatolia, while
110 compressional deformation to the east around the Bitlis–Zagros suture was explained by
111 collisional tectonics (e.g. Taymaz et al., 1990; Bozkurt, 2001) (Fig. 1). Central Anatolia is
112 located between an extensional regime to the west due to the subduction, and a compressional
113 regime to the east due to the collisional tectonics. There are several fault systems responsible
114 for ongoing seismic activity in the region. The major fault zone, the Central Anatolian Fault
115 Zone (CAFZ) (Fig. 2), which primarily represents a transtensional fault structure with a small
116 amount of left-lateral offset during the Miocene (e.g. Koçyiğit and Beyhan, 1998), can be
117 considered as a boundary between the carbonate nappes of the Anatolide-Tauride block and
118 the highly deformed and metamorphosed rocks in the Kırşehir block. To the northwest of the
119 CAFZ, Tuz Gölü Fault Zone (TGFZ) (Fig. 2), which is characterized by a right-lateral strike
120 slip motion with a significant oblique-slip normal component, appears to be collocated with
121 the Tuz Gölü Basin sedimentary deposits as well as the crystalline rocks within the Kırşehir
122 Block (e.g. Çemen et al., 1999; Bozkurt et al., 2001; Taymaz et al., 2004; Çubuk et al., 2014).
123 At the southwest tip of the study region, the EAFZ generates large seismic activity that can be
124 identified by rather complicated seismotectonic setting: predominantly left-lateral strike-slip
125 motion that is well correlated with the regional deformation pattern and with existing local

126 clusters of thrust and normal faulting events on NS- and EW-trending subsidiary faults,
127 respectively (Bulut et al., 2012). Such complicated behavior explains kinematic models (e.g.
128 Riedel shear, anti-Riedel shear models) of the shear deformation zone evolution (Tchalenko,
129 1970). It connects to the NAFZ at the Karlıova Triple Junction (Bozkurt, 2001) and to the
130 south splits into various segments nearby the Adana Basin (Kaymakci et al., 2006) (Fig. 2).
131 Toward the south, the EAFZ reaches the Dead Sea Fault Zone (DSFZ) that has a key role in
132 accommodating northward relative motions of Arabian and African Plates with respect to
133 Eurasia.

134

135 3. *Data*

136 The present work utilizes three-component waveforms of local seismic activity detected at 72
137 broadband seismic stations (Fig. 2) that have been operated for 2 years between 2013 and
138 2015 within the framework of a temporary passive seismic experiment, the Continental
139 Dynamics–Central Anatolian Tectonics (CD-CAT) (Portner et al., 2018). We benefit from
140 revisited standard earthquake catalogue information that is routinely released by the Kandilli
141 Observatory and Earthquake Research Institute (KOERI) (publicly available at
142 <http://www.koeri.boun.edu.tr>) to extract waveform data for a total of 2231 examined events
143 with station-event pair distance less than 120 km and focal depths less than 10 km. Most of
144 the detected seismic activity in the study area is associated to several fault zones in the region,
145 i.e., the EAFZ, CAFZ, DSFZ, TGFZ, etc. Here we note that the use of only local earthquakes
146 is to exclude possible biases, which may be introduced by Moho boundary guided Sn-waves.
147 Upper crustal earthquakes with less than 10 km focal depths are preferred in this study to
148 exclude effect of relatively large-scale heterogeneities on coda wave trains. Additionally, we
149 performed a visual inspection over all waveforms to ensure high-quality waveforms. Our final

150 event number reduced to 1193. Selected station and event distributions can be seen in Figure
151 2.

152

153 Observed waveforms were prepared at 5 different frequency bands with central frequencies at
154 0.75, 1.5, 3.0, 6.0, 12.0 Hz via a Butterworth band-pass filtering process. In the next step, we
155 applied Hilbert transform to filtered waveform data in order to obtain the total energy
156 envelopes. An average crustal velocity model was used to predict P and S wave onsets on
157 envelopes and then based on this information: (i) the noise level prior to the P-wave onset was
158 eliminated (ii) S-wave window was determined starting at 3s prior to and 7 s afterwards S-
159 wave onset as this allowed to include all direct S-wave energy, (iii) starting at the end of the
160 S-wave window, a coda window of 100s at maximum was determined. Length of coda
161 windows can be shorter when signal-to-noise ratio (SNR) is less than 2.5 or when there are
162 coda waves from two earthquakes (e.g. because of an aftershock sequence) within the same
163 analysis window, which can cause another rise instead of a decline in the envelope. We omit
164 the earthquakes with less than 10 s of coda length from our database. Taking into account of
165 these criteria, finally coda waveforms extracted from 6541 source-receiver pairs were used for
166 further data process.

167

168 *4. Method*

169 We adopted an inversion procedure that was originally developed by Sens-Schönfelder and
170 Wegler (2006) and later modified by Eulenfeld and Wegler (2016). The forward part, which
171 involves calculation of energy density for a specific frequency band under assumption of an
172 isotropic source, is expressed in Sens-Schönfelder and Wegler (2006) as follows:

$$173 \quad E_{mod}(t, r) = WR(r)G(t, r, g)e^{-bt} \quad (1)$$

174

175 where W gives source term and it is frequency dependent. $R(r)$ indicates the energy site
 176 amplification factor and b is intrinsic attenuation parameter. $G(t, r, g)$ represents Green's
 177 function that includes scattered wave field as well as direct wave and its expression is given
 178 by Paasschens (1997) as follows:

$$179 \quad G(t, r, g) = e^{(-v_0 t g_0)} \left[\frac{\delta(r - v_0 t)}{4\pi r^2} + \left(\frac{4\pi v_0}{3g_0} \right)^{-\frac{3}{2}} t^{-\frac{3}{2}} \times \left(1 - \frac{r^2}{v_0^2 t^2} \right)^{\frac{1}{8}} K \left(v_0 t g_0 \left(1 - \frac{r^2}{v_0^2 t^2} \right)^{\frac{3}{4}} \right) H(v_0 t - r) \right] \quad (2)$$

181 Here the term within Dirac delta function represents direct wave and other term indicates
 182 scattered waves. v_0 describes the mean S-wave velocity while g_0 is the scattering coefficient.

183 Possible discrepancy between predicted (Eq. 1) and observed energy densities for each event
 184 at each station with N_{ij} time samples (index k) in a specific frequency band can be minimized
 185 using:

$$187 \quad \epsilon(g) = \sum_{i,j,k}^{N_S, N_E, N_{ij}} (\ln E_{ijk}^{obs} - \ln E_{ijk}^{mod}(g))^2 \quad (3)$$

189 Here, the number of stations (index i) and events (index j) are shown by N_S and N_E ,
 190 respectively. Optimization of g will be achieved by fulfilling following equality:

$$192 \quad \ln E_{ijk}^{obs} = \ln E_{ijk}^{mod} \quad (4) \quad \text{or}$$

$$194 \quad \ln E_{ijk}^{obs} = \ln G(t_{ijk}, r_{ijk}, g) + \ln R_i + \ln W_j - b t_{ijk} \quad (5)$$

195 Equation 5 simply define an overdetermined inversion problem with $\sum_{i,j} N_{ij}$ number equation

196 systems and with $N_S + N_E + 1$ variables and thus b , R_i , and W_j can be solved via a least-
197 squares technique. $\epsilon(g)$ can be defined as sum over the squared residuals of the solution. As
198 can be seen from equation 1 that there is an obvious trade-off between R_i and W_j , which we
199 can manage by fixing the geometrical mean of R_i to 1 ($\prod R_i = 1$). Equation 1 also implies
200 rather moderate trade-off between W_j and b . Trade-off between g and other inverted
201 parameters are usually small since this parameter is fixed through the energy ratio of the
202 direct S-wave and the level of the coda-waves (Gaebler et al., 2018).

203 Eulenfeld and Wegler (2016) present a simple recipe to perform the inversion:

204 (i) Calculate Green's functions through the analytic approximation of the solution for 3-D
205 isotropic radiative transfer (e.g. Paasschens 1997; Sens-Schönfelder and Wegler, 2006) by
206 using fixed scattering parameters and minimize equation 5 to solve for b , R_i , and W_j via a
207 weighted least-squares approach.

208 (ii) Calculate $\epsilon(g)$ using equation 3.

209 (iii) Repeat (i) and (ii) by selecting different g to find the optimal parameters g , b , R_i and W_j
210 that finally minimize the error function ϵ .

211 In Fig. 3 an example for the minimization process that was applied at five different frequency
212 bands is displayed for one selected event at recorded stations of the CD-CAT project.

213 Minimization described above for different frequencies will yield unknown spectral source
214 energy term, W_j as well as site response, R_i and attenuation parameters, b , and g that will
215 satisfy optimal fitting between observed and predicted coda wave envelopes. Example for this
216 fitting can be seen in Figure 4. The present study deals with frequency dependency of W_j
217 since this information can be later useful to obtain source displacement spectrum and thus

218 seismic moment and moment magnitudes of analyzed earthquakes using the formula of the *S*-
 219 wave source displacement spectrum for a double-couple source in the far-field, which is given
 220 by Sato et al. (2012):

$$221 \quad \omega M(f) = \sqrt{\frac{5\rho_0 v_0^5 W}{2\pi f^2}} \quad (6)$$

222 where W indicates the radiated *S*-wave energy at a center frequency f while v_0 and ρ_0
 223 represent the mean *S*-wave speed and medium density, respectively.

224 The relation between the obtained source displacement spectrum and seismic moment value
 225 was earlier described in Abercrombie (1995) by:

$$226 \quad \omega M(f) = M_0 \left(1 + \left(\frac{f}{f_c}\right)^{\gamma n}\right)^{-\frac{1}{\gamma}} \quad (7)$$

227 where n is related to the high-frequency fall-off and γ is known as shape parameter that
 228 controls the sharpness of spectrum at corner frequency between the constant level M_0 (low
 229 frequency part) and the fall-off with f^{-n} (high frequency part). Taking the logarithm of
 230 equation 7 gives:

231

$$232 \quad \ln \omega M(f) = \ln M_0 - \frac{1}{\gamma} \ln \left(1 + \left(\frac{f}{f_c}\right)^{\gamma n}\right) \quad (8)$$

233

234 Eq. 8 describes an optimization problem where the observed source displacement spectrum
 235 data (left-hand side) can be inverted for four unknown source parameters, M_0 , γ , n , and f_c
 236 (right-hand side) in a simultaneous least-squares inversion scheme. Finally moment
 237 magnitude, M_w can be calculated from modeled source parameters, seismic moment, M_0
 238 using a formula given by Hanks and Kanamori (1979):

239

240
$$M_w = \frac{2}{3} \log_{10} M_0 - 10.7 \quad (9)$$

241

242 *5. Results and Discussions*

243 *5.1 Coda wave source spectra*

244 Figure 5 displays observed values of source spectra established by inserting inverted spectral
245 source energy term W at each frequency in Eq. 6 for all analyzed events. Each curve in this
246 figure represents the model spectrum estimate based on the inversion procedure described in
247 the previous section. Modeled spectrum characteristics computed for 487 local earthquakes
248 whose geographical distribution is presented in Figure 2 suggest, in general, that we were able
249 to obtain typically expected source displacement spectrum with a flat region around the low
250 frequency limit and a decaying behaviour above a corner frequency.

251

252 Owing to the multiple-scattering process within small scale heterogeneities that makes coda
253 waves gain an averaging nature, the variation in coda amplitudes due to differences in source
254 radiation pattern and path effect are reduced (Walter et al., 1995; Mayeda et al., 2003).
255 Eulenfeld and Wegler (2016) found that radiation pattern would have only a minor influence
256 on the S-wave coda while it might disturb attenuation models inferred from the direct S-wave
257 analyses unless the station distribution relative to the earthquakes indicates a good azimuthal
258 coverage.

259

260 Conventional approaches (e.g. Abercrombie, 1995; Kwiatek et al., 2011) to estimate source
261 parameters such as corner frequency, seismic moment, high-frequency fall-off through fitting
262 of observed displacement spectra observed at a given station in an inversion scheme could be
263 misleading since these methods usually: (i) assume a constant value of attenuation effect (no
264 frequency variation) defined by a factor $\exp(-\pi f t Q^{-1})$ over the spectrum, (ii) and assume

265 omega-square model with a constant high-frequency fall-off parameter, $n=2$. Following Sens-
266 Schönfelder and Wegler (2006) and Eulenfeld and Wegler (2016), however, we estimate
267 attenuation parameters (intrinsic and scattering) separately within a simultaneous inversion
268 procedure in which high-frequency fall-off parameter varies. This is fairly consistent with
269 early studies (e.g. Ambeh and Fairhead, 1991; Eulenfeld and Wegler, 2016) where significant
270 deviations from the omega square model ($n>3$) were reported implying that the omega-square
271 model as a source model for small earthquakes must be reconsidered in its general
272 acceptance. Earlier it has been well-observed that the source spectra, especially, for large
273 earthquakes could be better explained by models of two corner frequencies (e.g.,
274 Papageorgiou and Aki, 1983; Joyner, 1984; Atkinson, 1990). Recently, Denolle et al. (2016)
275 observed that conventional spectral model of a single-corner frequency and high-frequency
276 fall-off rate could not explain P wave source spectra of thrust earthquakes with magnitude
277 M_w 5.5 and above. Instead, they suggested the double-corner-frequency model for large
278 global thrust earthquakes with a lower corner frequency related to source duration and with an
279 upper corner frequency suggesting a shorter time scale unrelated to source duration, which
280 exhibits its own scaling relation. Uchide and Imanishi (2016) reported similar differences
281 from the omega-square model would be valid also for smaller earthquakes by using spectral
282 ratio technique that involves empirical Green's function (EGF) events to avoid having a
283 complete knowledge of path and site effects for shallow target earthquakes (M_w 3.2–4.0) in
284 Japan. The source spectra for many of the target events in their study suggested a remarkable
285 discrepancy from the omega-square model for relatively small earthquakes. They explained
286 such differences by incoherent rupture due to heterogeneities in fault properties and applied
287 stress, the double-corner-frequency model, and possibility of a high-frequency falloff
288 exponent value slightly higher than 2. In our case, the smallest event was with M_w -coda
289 larger than 2.0, thus we had no chance to make a similar compared to that of Eulenfeld and

290 Wegler (2016). However, high-frequency fall-off parameters varied from $n=0.5$ to $n=4$. A
291 notable observation in the distribution of n was $n=2$ or $n=2.5$ would be better explained for
292 earthquakes with $M_W\text{-coda} > 4.0$ whereas the smaller magnitudes exhibited more scattered
293 pattern of variation in n (Figure 7). Eulenfeld and Wegler (2016) claimed that the use of
294 separate estimates of the attenuation or correction for path effect via empirically determined
295 Green's function would be better strategy in order to invert station displacement spectra for
296 source parameters. This is mainly because smaller earthquakes (with $n > 2$), in particular,
297 assuming omega-square model can distort the estimates of corner frequency and even seismic
298 moment especially in regions where Q is strongly frequency dependent. Thus, independent
299 estimates of Q during station displacement spectra inversions for source parameters must be
300 taken into account or the influence of path such as attenuation must be removed via
301 empirically determined Green's functions (Eulenfeld and Wegler, 2016).

302

303 *5.2 Coda wave-derived magnitude vs. M_L catalogue magnitude*

304 A scatter plot between catalogue magnitudes based on local magnitudes (M_L) and our coda-
305 derived magnitudes ($M_W\text{-coda}$) that are inferred from resultant frequency dependent source
306 displacement spectra and thus seismic moment (e.g. Eq. 9) is shown in Fig. 6. Such
307 comparison suggests an overall coherency between both types of magnitudes. This implies
308 that a very simple model of a first-order approximation for S-wave scattering with isotropic
309 acoustic radiative transfer approach can be efficient to link the amplitude and decaying
310 character of coda wave envelopes to the seismic moment of the source.

311

312 In the present study, a linear regression analyses performed between $M_W\text{-coda}$ and M_L
313 magnitudes (Fig. 5) resulted in an empirical formula that can be employed to convert local

314 magnitudes into coda-derived moment magnitude calculation of local earthquakes in this
315 region:

316

$$317 \quad M_{W-coda} = 1.1655 \pm 0.0337 \times M_L - 0.7085 \pm 0.0128 \quad (10)$$

318

319 Bakun and Lindh (1977) empirically described the linear log seismic moment-local
320 magnitude relation between seismic moments (M_0) and local magnitudes (M_L) for
321 earthquakes near Oroville, California. Beside this several other studies investigated to find an
322 optimum relation between M_W and M_L by implementing linear and/or non-linear curve-fitting
323 approaches. Malagnini and Munafò (2018) proposed two different linear fits separated by a
324 crossover $M_L=4.31$ could represent M_L - M_W data points obtained from earthquakes of the
325 central and northern Apennines, Italy. Several coefficient of regression analyses in their fits
326 account for the combined effects of source scaling and crustal attenuation as well as regional
327 attenuation, focal depth, and rigidity at source. Goertz-Allmann et al. (2011), for instance,
328 introduced hybrid type of scaling relation that is linear below M_L 2 and above M_L 4 and a
329 quadratic relation in between ($2 \leq M_L \leq 4$) for earthquakes in Switzerland detected between
330 1998 and 2009. Edwards and Rietbrock (2009) employed a second-order polynomial equation
331 to relate local magnitudes routinely reported in the Japan Meteorological Agency (JMA)
332 magnitude and moment magnitude. More recently, using multiple spectral ratio analyses
333 Uchide and Imanishi (2018) estimated relative moment magnitudes for the Fukushima
334 Hamadori and the northern Ibaraki prefecture areas of Japan and reported a quadratic form of
335 correlation between JMA magnitudes and moment magnitudes. Resultant empirical curve in
336 Uchide and Imanishi (2018) implied a considerable discrepancy between the moment
337 magnitudes and the JMA magnitudes, with a slope of 1/2 for microearthquakes suggesting

338 possible biases introduced by anelastic attenuation and the recording by a finite sampling
339 interval.

340

341 Apparent move-out in Fig. 5 and Eq. 10, presumably stems from the use of different
342 magnitude scales for comparison. Conventional magnitudes scales such as M_L , mb inferred
343 from phase amplitude measurements are seemingly sensitive to attenuation and 2D variation
344 along the path (Pasyanos et al., 2016). Unlike local magnitude scales, seismic moment-based
345 moment magnitude (M_W) essentially represents a direct measure of the strength of an
346 earthquake caused by fault slip and is estimated from relatively flat portion of source spectra
347 at lower frequencies that can be less sensitive to the near surface attenuation effects. The
348 consistency between coda-derived moment magnitude and local magnitude scales for the
349 earthquakes with $M_{W-coda} > 3.0$ indicates that our non-empirical approach successfully
350 worked in this tectonically complex region. This observation is anticipated, for relatively
351 large earthquakes, since more energy will be characteristic at lower frequencies. We
352 observed similar type of consistency in early studies that investigate source properties of local
353 and regional earthquakes based on empirical coda methods with simple 1-D radially
354 symmetric path correction (e.g. Eken et al., 2004; Gök et al., 2016). Coda waves-derived
355 source parameters were obtained with high-precision in Mayeda et al. (2005), Phillips et al.
356 (2014), Pasyanos et al. (2016) following the use of 2-D path-corrected station techniques to
357 consider the amplitude-distance relationships. Observable outliers in Figure 5, for the events
358 with less than M_w 3.5, however, can be attributed to the either possible biases on local
359 magnitude values taken from the catalogue or small biases on our intrinsic (Q_i^{-1}) and
360 scattering (Q_s^{-1}) attenuation terms. One another possible contribution to such mismatch might
361 be associated to the influences of mode conversions between body and surface waves or

362 surface-to-surface wave scattering that are not restricted to low frequencies ($<1\text{Hz}$) (Sens-
363 Schönfelder and Wegler, 2006).

364

365 *6. Conclusions*

366 This study provides moment magnitude estimates as a direct physical measure of the seismic
367 energy for local earthquakes with magnitudes $2.0 \leq M_L \leq 5.2$ recorded at 69 seismic stations
368 in central Anatolia. The source displacement spectra were obtained following the application
369 of a coda wave modeling procedure that employs a simultaneous optimization of source, path,
370 and site specific terms by fitting physically derived synthetic coda envelope and observed
371 coda envelopes. The Radiative Transfer Theory was used for analytic expression of synthetic
372 coda wave envelopes. Overall consistency between M_w -coda and M_L suggests that our non-
373 empirical approach successfully worked in this tectonically complex region. Variation of
374 high-frequency fall-off parameter indicated that for smaller earthquakes ($n > 2$) assuming
375 omega-square model can distort the estimates of corner frequency and even seismic moment
376 especially in regions where Q is strongly frequency dependent. Since the present study mainly
377 focuses on source properties of local earthquakes in the study area, scattering and intrinsic
378 attenuation properties that are other products of our coda envelope fitting procedure will be
379 examined in details within a future work. Finally, a linear regression analysis resulted in an
380 empirical relation developed between M_w -coda and M_L , which will be a useful tool in the
381 future to quickly convert catalogue magnitudes into moment magnitudes for local earthquakes
382 in the study area.

383

384 *Data and resources*

385 The python code used for carrying out the inverse modeling is available under the permissive
386 MIT license and is distributed at <https://github.com/trichter/qopen>. We are grateful to the IRIS

387 Data Management Center for maintaining, archiving and making the continuous broadband
388 data used in this study open to the international scientific community. The KOERI is specially
389 thanked for providing publicly open local seismicity catalogues.

390

391 *Acknowledgement*

392 The facilities of IRIS Data Services, and specifically the IRIS Data Management Center, were
393 used for access to waveforms, related metadata, and/or derived products used in this study.
394 IRIS Data Services are funded through the Seismological Facilities for the Advancement of
395 Geoscience and EarthScope (SAGE) Proposal of the National Science Foundation under
396 Cooperative Agreement EAR-1261681. Data for the CD-CAT experiment
397 (https://doi.org/10.7914/SN/YB_2013) are available from the IRIS Data Management Center
398 at <http://www.iris.edu/hq/>. Tuna Eken acknowledge financial support from Alexander von
399 Humboldt Foundation (AvH) towards computational and peripherals resources. I am grateful
400 to the Topical Editor Charlotte Krawczyk for handling the revision process and Takahiko
401 Uchide and Ludovic Margerin for their valuable opinions on the improvement of manuscript.

402 *References*

- 403 Abercrombie, R.E.: Earthquake source scaling relationships from -1 to 5 ML using
404 seismograms recorded at 2.5-km depth, *J. geophys. Res.*, 100(B12), 24 015–24 036,
405 1995.
- 406 Aki, K., and Chouet., B.: Origin of coda waves: Source, attenuation, and scattering effects, *J.*
407 *Geophys. Res.* 80, 3322–3342, 1975.
- 408 Atkinson, G. M.: A comparison of eastern North American ground motion observations with
409 theoretical predictions, *Seismol. Res. Lett.* 61, 171–180, 1990.

410 Bakun, W.H. and Lindh, A.G.: Local Magnitudes, Seismic Moments, and Coda Durations for
411 Earthquakes Near Oroville, California, Bulletin of the
412 Seismological Society of America. Vol.67, No.3, pp. 615-629, 1977.

413 Bozkurt, E.: Neotectonics of Turkey—A synthesis: *Geodinamica Acta*, v. 14, p. 3–30, 2001.

414 Bulut, F., Bohnhoff, M., Eken, T., Janssen, C., Kılıç, T., and Dresen, G.: The East Anatolian
415 fault zone: Seismotectonic setting and spatiotemporal characteristics of seismicity based
416 on precise earthquake locations: *Journal of Geophysical Research*, v. 117, B07304,
417 <https://doi.org/10.1029/2011JB008966>, 2012.

418 Çemen, I., Göncüoğlu, M.C., and Dirik, K.: Structural evolution of the Tuz Gölü basin in central
419 Anatolia, Turkey: *Journal of Geology*, v. 107, p. 693–706, <https://doi.org/10.1086/314379>, 1999.

421 Çubuk Y, Yolsal-Çevikbilen S, Taymaz, T.: Source parameters of the 20052008 Balıkesir (central Turkey) earthquakes: Implications for the internal deformation of the Anatolian
422 plate. *Tectonophysics* 635(Supplement C) :125 – 153, 2014.

424 Denolle, M. A., and Shearer, P.M.: New perspectives on self-similarity for shallow thrust
425 earthquakes, *J. Geophys. Res. Solid Earth*, 121, 6533–6565, 2016.

426 Edwards, B., & Rietbrock, A.: A comparative study on attenuation and source-scaling relations
427 in the Kantō, Tokai, and Chubu regions of Japan, using data from Hi-net and KiK-net.
428 *Bulletin of the Seismological Society of America*, 99, 2435–2460, 2009.

429 Eken, T., Mayeda, K., Hofstetter, A., Gök, R., Orgülü, G. and Turkelli, N.: An application of the
430 coda methodology for moment-rate spectra using broadband stations in Turkey.
431 *Geophys. Res. Lett*, 31, L11609, 2004.

432 Eulenfeld, T. and Wegler, U.: Measurement of intrinsic and scattering attenuation of shear
433 waves in two sedimentary basins and comparison to crystalline sites in Germany,
434 *Geophys J Int.*, 205(2):744-757, 2016.

435 Eulenfeld, T. and Wegler, U.: Crustal intrinsic and scattering attenuation of high-frequency
436 shear waves in the contiguous United States. *J Geophys., Res*, 122, 2017.

437 Favreau, P., and Archuleta, R.J.: Direct seismic energy modelling and application to the 1979
438 Imperial Valley earthquake, *Geophys. Res. Lett.*, 30, 1198, 2003.

439 Gaebler, P.J., Eulenfeld, T. & Wegler, U.: Seismic scattering and absorption parameters in the
440 W-Bohemia/Vogtland region from elastic and acoustic radiative transfer theory,
441 *Geophys. J. Int.*, 203(3), 1471–1481, 2015.

442 Gaebler, P.J., Eken, T., Bektaş, H.Ö, Eulenfeld, T., Wegler, U., Taymaz, T.: Imaging of Shear
443 Wave Attenuation Along the Central Part of the North Anatolian Fault Zone, Turkey,
444 submitted to the *Journal of Seismology*, 2018.

445 Goertz-Allmann, B. P., Edwards, B., Bethmann, F., Deichmann, N., Clinton, J., Fäh, D., &
446 Giardini, D.: A new empirical magnitude scaling relation for Switzerland. *Bulletin of the*
447 *Seismological Society of America*, 101, 3088–3095, 2011.

448 Gök, R., Kaviani, A., Matzel, E. M., Pasyanos, M. E., Mayeda, K., Yetirmishli, G., El-Hussain,
449 I., Al-Amri, A., Al-Jeri, F., Godoladze, T., Kalafat, D., Sandvol, E. A., and Walter,
450 W.R.: Moment Magnitudes of Local/Regional Events from 1D Coda Calibrations in the
451 Broader Middle East Region. *Bull Seismol Soc Am.*, 106(5):1926-1938, 2016.

452 Gusev, A.A. & Abubakirov, I.R.: Simulated envelopes of non-isotropically scattered body
453 waves as compared to observed ones: another manifestation of fractal heterogeneity,
454 *Geophys. J. Int.*, 127(1), 49–60, 1996.

455 Hanks, T.C. and Kanamori, H.: A moment magnitude scale, *J. Geophys., Res.*, 84, 2348–2350,
456 1979.

457 Izgi, G., Eken, T., Gaebler, P., and Taymaz, T.: Frequency-Dependent Shear Wave Attenuation
458 Along the Western Part of the North Anatolian Fault Zone, Geophysical Research
459 Abstracts, Vol. 20, EGU2018-629-2, 2018.

460 Kaymakci, N. Inceöz, M. Ertepinar, P.: 3D architecture and Neogene evolution of the Malatya
461 Basin: inferences for the kinematics of the Malatya and Ovacik Fault Zones. Turkish
462 Journal of Earth Sciences, 15, 123-154, 2006.

463 Kwiatek, G., Plenkers, K. & Dresen, G.: 2011. Source parameters of pico-seismicity recorded at
464 Mponeng Deep Gold Mine, South Africa: implications for scaling relations, Bull. seism.
465 Soc. Am., 101(6), 2592–2608, 2011.

466 Malagnini, L., Mayeda, K., Akinci, A., and Bragato, P. L.: Estimating absolute site effects,
467 Bull. Seismol. Soc. Am. 94, no. 4, 1343–1352, 2004.

468 Malagnini, L., and Munafò, I.: On the Relationship between M_L and M_w in a Broad Range: An
469 Example from the Apennines, Italy, Bulletin of the Seismological Society of America,
470 Vol. 108, No. 2, pp. 1018–1024, 2018.

471 Mayeda, K., and Walter, W.R.: Moment, energy, stress drop, and source spectra of western
472 United States earthquakes from regional coda envelopes, J. Geophys. Res. 101, 11,195–
473 11,208, 1996.

474 Mayeda, K., Hofstetter, A., O’Boyle, J.L., and Walter, W.R.: Stable and transportable regional
475 magnitudes based on coda-derived moment-rate spectra, Bull. Seismol. Soc. Am. 93,
476 224–239: 2003.

477 Mayeda, K., Malagnini, L., Phillips, W. S., Walter, W. R., and Dreger, D.: 2D or not 2D, that is
478 the question: A Northern California Test. Geophysical Research Letters, 32(12), 2005.

479 Morasca, P., Mayeda, K., Malagnini, L. and Walter, W.R.: Coda and direct-wave attenuation
480 tomography in northern Italy, Bull Seismol Soc Am., v. 98, pages, 1936-1946, 2004.

481 Morasca, P., Mayeda, K., Gök, R., Phillips, W.S., and Malagnini, L.: Coda-derived source
482 spectra, moment magnitudes and energy-moment scaling in the western Alps, *Geophys.*
483 *J. Int.*, 160, 263–275, 2008.

484 Paasschens, J.: Solution of the time-dependent Boltzmann equation, *Phys. Rev. E*, 56(1), 1135–
485 1141, 1997.

486 Papageorgiou, A., and Aki, K.: A specific barrier model for the quantitative description of
487 inhomogeneous faulting and the prediction of strong ground motion I: Description of the
488 model, *Bull. Seismol. Soc. Am.*, 73(3), 693–722, 1983.

489 Pasyanos, M. E., R. Gök, and Walter, W.R.: 2-D variations in coda amplitudes in the Middle
490 East. *Bull. Seismol. Soc. Am.* 106, no. 5, 2016.

491 Phillips, W. S., Mayeda, K. M., and Malagnini, L.: How to invert multi-band, regional phase
492 amplitudes for 2-d attenuation and source parameters: Tests using the usarray. *Pure and*
493 *Applied Geophysics*, 171(3):469-484, 2014.

494 Portner, D.E., Delph, J.R., Biryol, C.B., Beck, S.L., Zandt, G., Özacar, A.A., Sandvol, E., and
495 Türkelli, N.: Subduction termination through progressive slab deformation across
496 Eastern Mediterranean subduction zones from updated P-wave tomography beneath
497 Anatolia, *Geosphere*, 14(3): 907-925, 2018.

498 Przybilla, J. and Korn, M.: Monte Carlo simulation of radiative energy transfer in continuous
499 elastic random mediathree-component envelopes and numerical validation. *Geophys J*
500 *Int* , 173(2):566-576, 2008.

501 Rautian, T.G. & Khalturin, V.I.: The use of the coda for determination of the earthquake source
502 spectrum, *Bull. Seism. Soc. Am.*, 68(4), 923–948, 1978.

503 Sato, H. and Fehler, M.C.: *Seismic Wave Propagation and Scattering in the Heterogeneous*
504 *Earth*, Springer-Verlag, New York, 1998.

505 Sato, H., Fehler, M.C. & Maeda, T. Seismic Wave Propagation, and Scattering in the
506 Heterogeneous Earth, 2nd edn, Springer: 2012.

507 Sens-Schönfelder, C. and Wegler, U.: Radiative transfer theory for estimation of the seismic
508 moment. *Geophys J Int*, 167(3):1363-1372.

509 Taymaz, T., Jackson, J., Westaway, R.: Earthquake mechanisms in the Hellenic Trench near
510 Crete. *Geophys. J. Int.*102, 695–731, 1990.

511 Taymaz, T., Westaway, R., Reilinger, R.: Active faulting and crustal deformation in the eastern
512 Mediterranean Region. *Spec. Issue Tectonophys.* 391 (1-4), 1–9. [http://](http://dx.doi.org/10.1016/j.tecto.2004.07.005)
513 dx.doi.org/10.1016/j.tecto.2004.07.005, 2004.

514 Tchalenko, J. S.: Similarities between shear zones of different magnitudes. *Geol. Soc. Am.*
515 *Bull.*, 81, 1625–1640, 1970.

516 Uchide, T., & Imanishi, K.: Small earthquakes deviate from the omega-square model as revealed
517 by multiple spectral ratio analysis. *Bulletin of the Seismological Society of America*,
518 106(3), 1357–1363, 2016.

519 Uchide, T., & Imanishi, K.: Underestimation of microearthquake size by the magnitude scale of
520 the Japan Meteorological Agency: Influence on earthquake statistics. *Journal of*
521 *Geophysical Research: Solid Earth*, 123, 606–620, 2018.

522 Yoo, S.-H., Rhie, J., Choi, H.-S., and Mayeda, K.: Coda-derived source parameters of
523 earthquakes and their scaling relationships in the Korean Peninsula, *Bull. Seismol. Soc.*
524 *Am.*, 101, 2388–2398, 2011.

525 Zeng, Y., Su, F. and Aki, K.: Scattering wave energy propagation in a random isotropic
526 scattering medium: 1. Theory, *J. Geophys. Res.*, 96(B1), 607–619, 1991.

527

528

529

530 *Figure Captions*

531 Figure 1. Major tectonic features of Turkey and its adjacent. The plate boundary data used
532 here is taken from Bird (2003). Subduction zones are black, continental transform faults are
533 red, continental rift boundaries are green, and spreading ridges boundaries are yellow. NAFZ,
534 EAFZ, and DSFZ are the North Anatolian Fault, East Anatolian Fault, and the Dead Sea fault,
535 respectively.

536

537 Figure 2. Epicentral distribution of all local events selected from the study area in the KOERI
538 catalogue. Gray circles represent earthquakes with poor quality that are not considered for the
539 current study while black indicates the location of local events with good quality. Red circles
540 among these events are 487 events used in coda wave inversion since they are successful at
541 passing quality criteria of further pre-processing procedure.

542

543 Figure 3. An example from the inversion procedure explained in chapter 3. Here coda
544 envelope fitting optimization is performed on band-pass filtered (4-8Hz) digital recordings of
545 an earthquake (2014 April 09, M_W -coda3.2) extracted for 7 seismic stations that operated
546 within the CD-CAT array. Large panel at the lower left-hand side displays the error function ϵ
547 as a function of g_0 . Thick blue cross here represent the optimal value of $g = g_0$. Other small
548 panels at upper and right-hand side show the least- squares solution of the weighted linear
549 equation system for the first 6 guesses and optimal guess for g_0 . The dots and gray curves
550 indicate the ratio between energy (E^{obs}) and the Green's function (G) obtained for direct S-
551 waves and observed envelopes at various stations, respectively (Please notice that during this
552 optimization process envelopes are corrected for the obtained site corrections R_i). The slope
553 of linear curve at each small panel yields $-b$ in relation to the intrinsic attenuation. The linear

554 curve has an intercept of W representing source related terms at the right-hand side of
555 equation 5.

556

557 Figure 4. a) Results of the inversion of the 2014-April-09, M_W -coda3.2 earthquake: Sample
558 fits between observed and calculated energy densities in the frequency band 0.5–1.0 Hz are
559 given for 6 different stations (see upper right corner for event ID, station name, and distance
560 to hypocenter). Note that light blue curves represent observed envelope. Smoothed observed
561 calculated envelopes in each panel are presented by blue and red curves, respectively. Blue
562 and red dots exhibit location of the average value for observed and calculated envelopes
563 within the S-wave window, respectively. b) The same as in (a) obtained in the frequency band
564 4.0–8.0 Hz.

565

566 Figure 5. All individual observed (black squares) and predicted (gray curve) source
567 displacement spectra observed at 72 stations from 487 local earthquakes in central Anatolia.

568

569 Figure 6: Scatter plot between local magnitudes (M_L) of analyzed events with coda waves-
570 derived magnitudes (M_W -coda) of the same events. The outcome of a linear regression
571 analysis yielded an empirical formula (e.g. Eq. 10) to identify the overall agreement
572 represented by gray straight line. Yellow and red dashed lines indicate upper and lower limit
573 of linearly fitting to that scatter.

574

575 Figure 7: Same scatter plot displayed in Fig. 6. Here color code indicates estimated high-
576 frequency fall-off parameter for each inverted event.

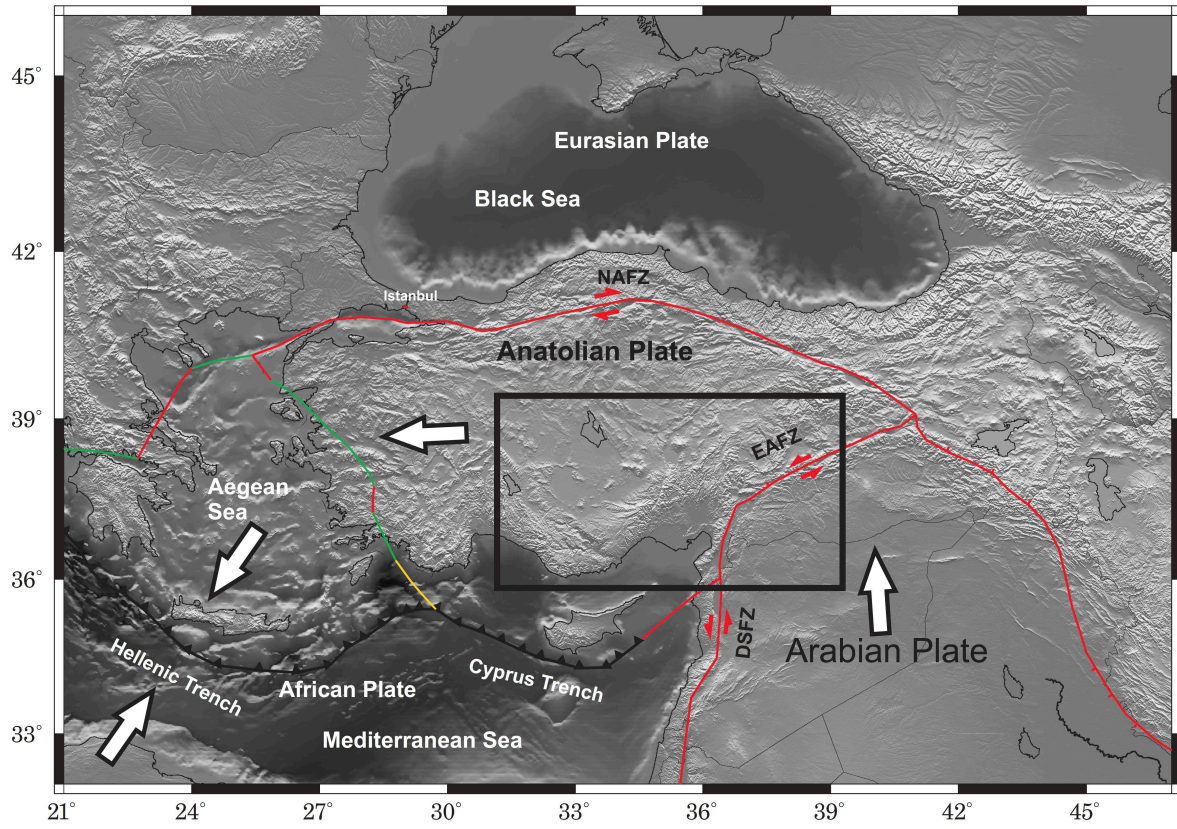
577

578

579

580

581



582

583

584

585 Figure 1.

586

587

588

589

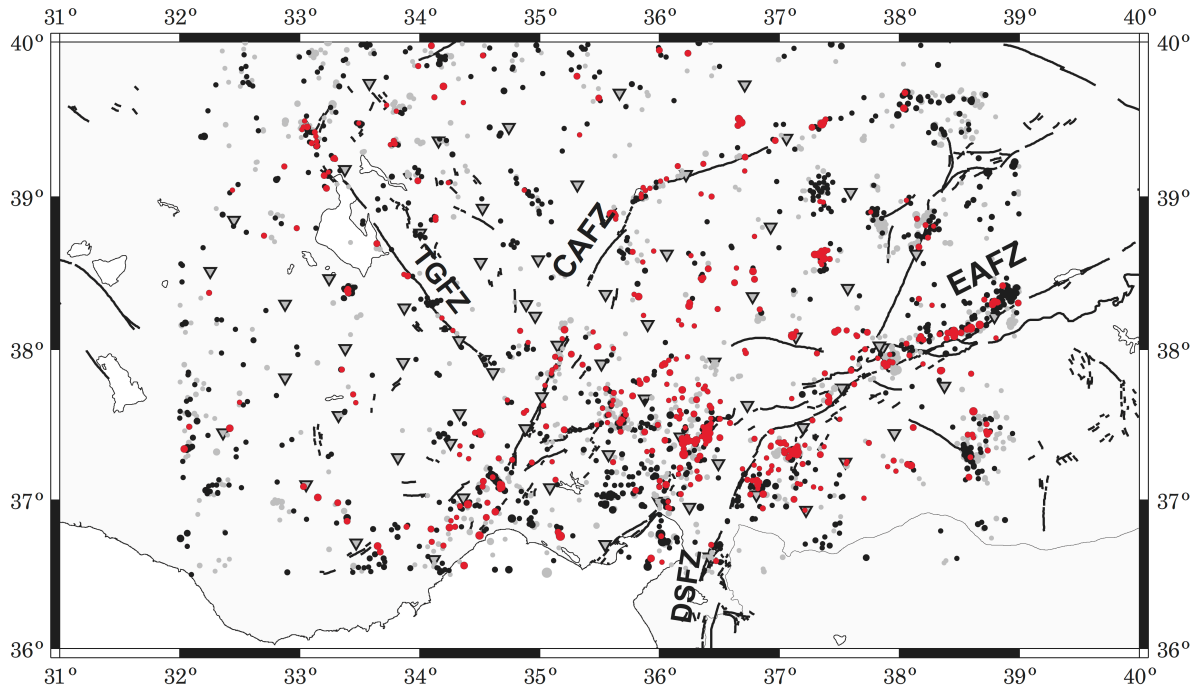
590

591

592

593

594



595

596 Figure 2.

597

598

599

600

601

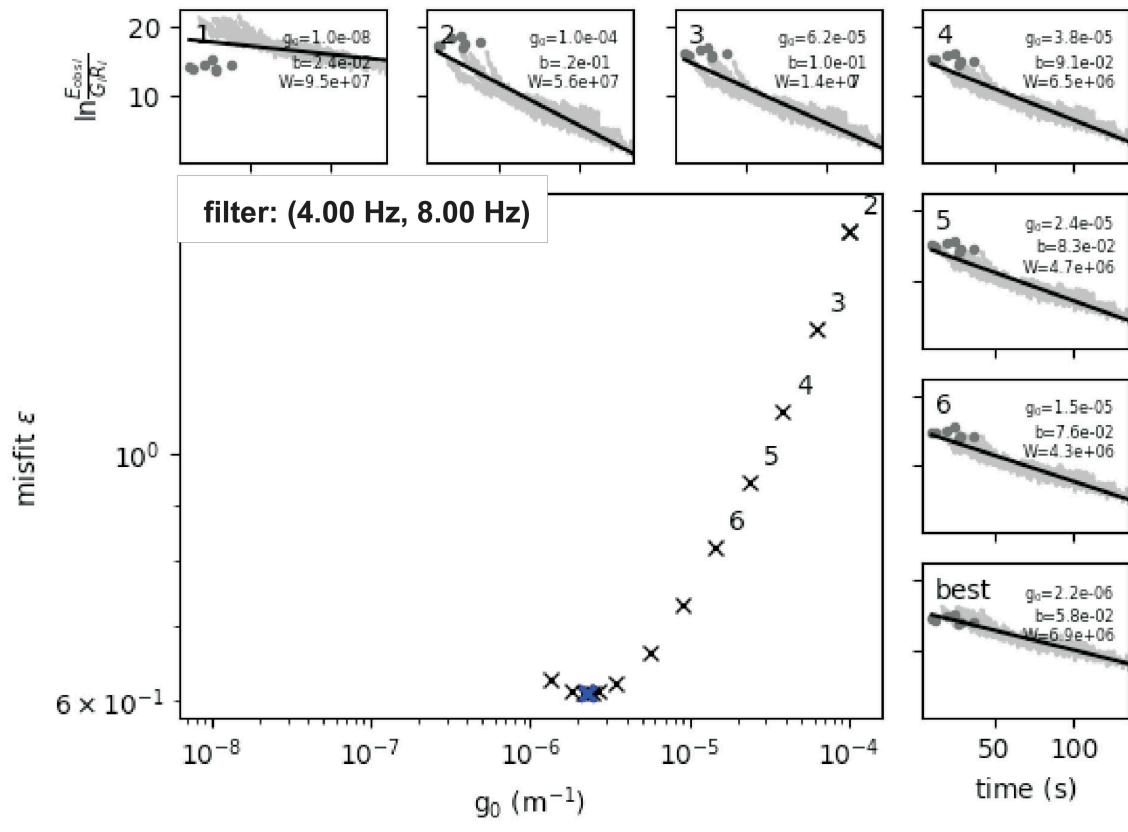
602

603

604

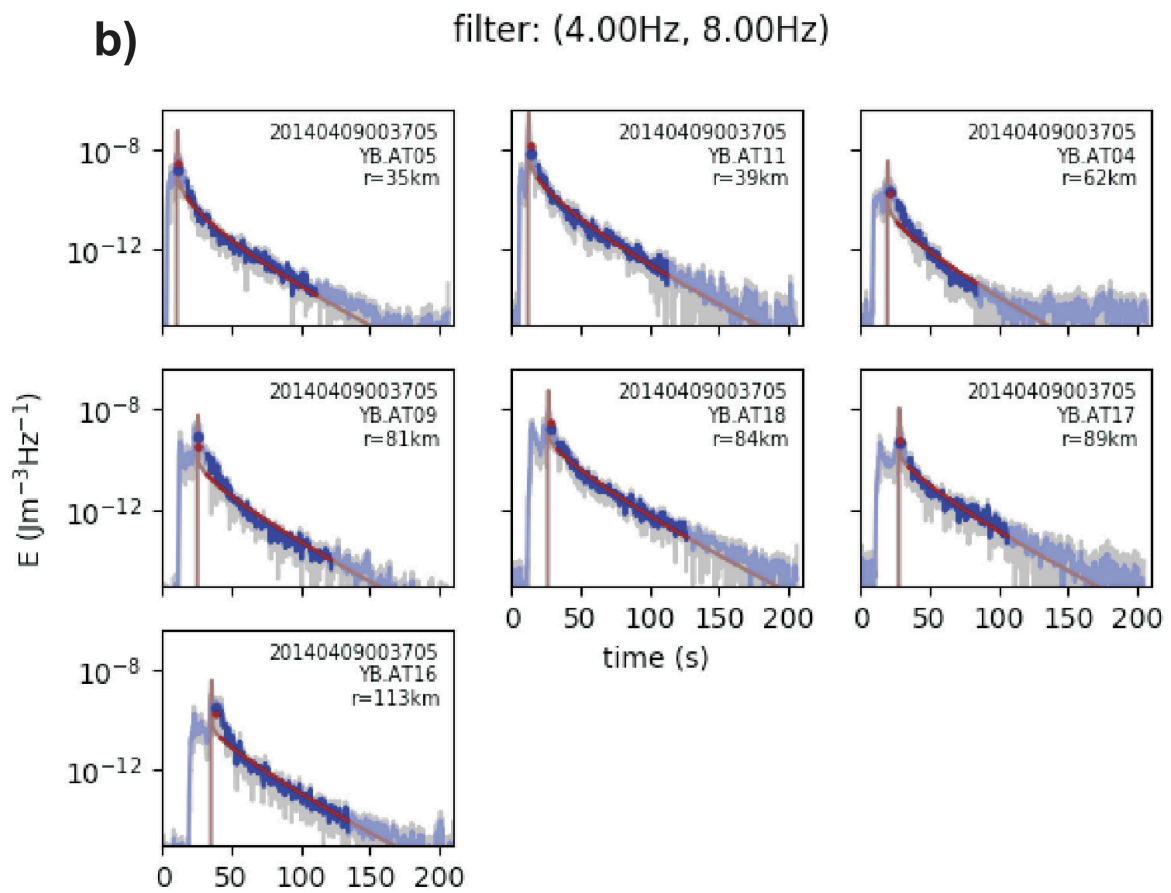
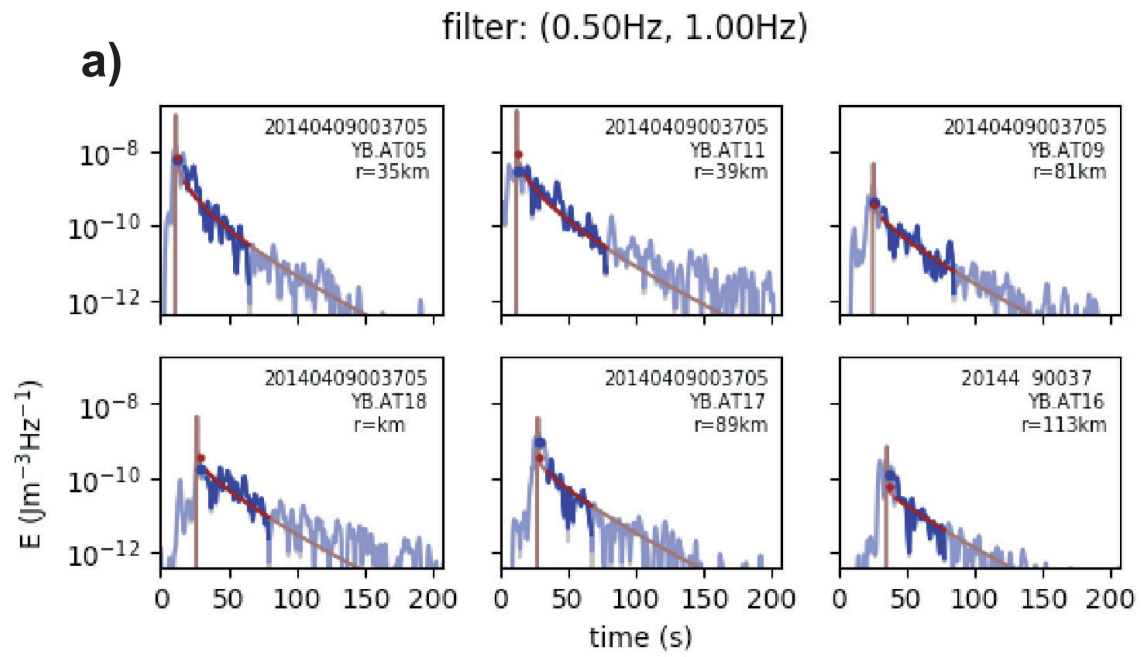
605

606



607
608
609
610
611

Figure 3.



612

613

614

615

616

617

618

Figure 4.

619
620
621
622
623

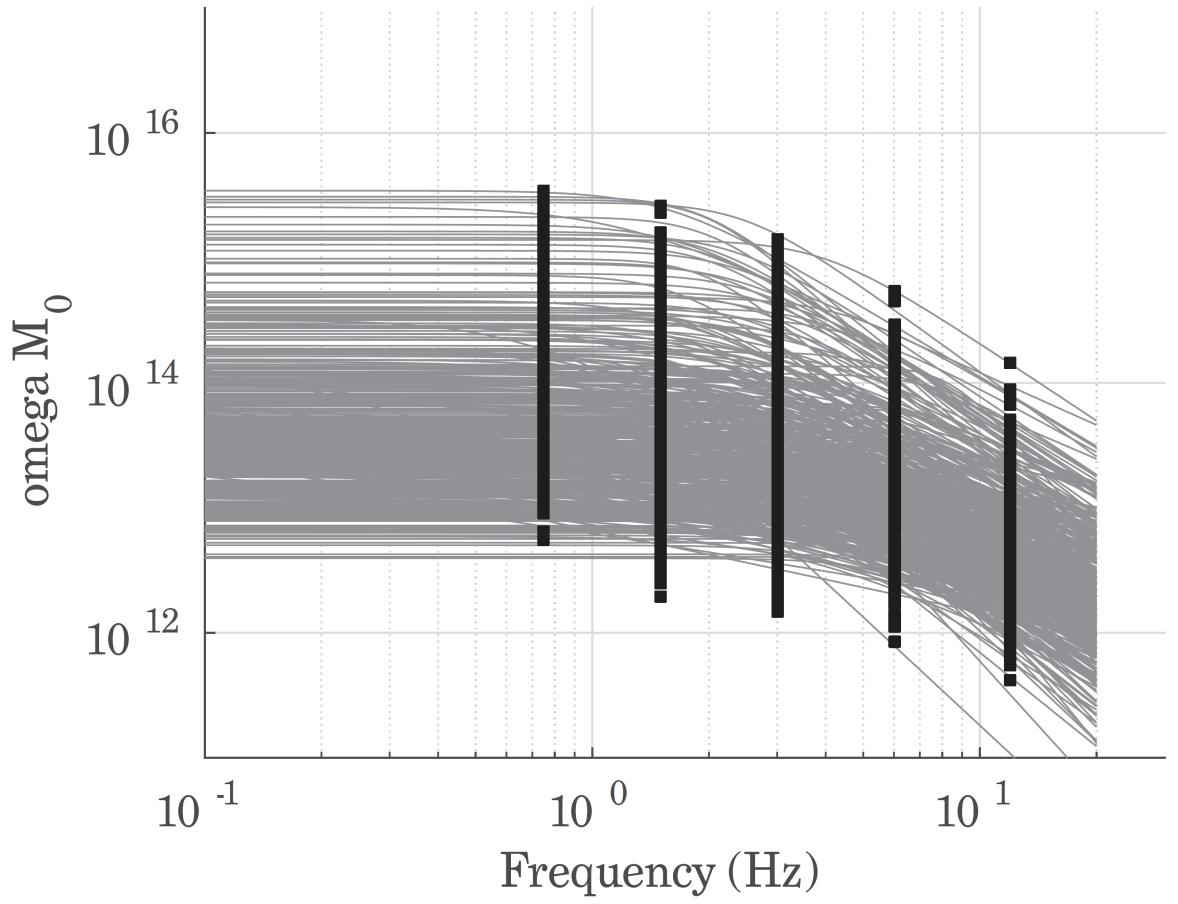


Figure 5.

624
625
626
627
628
629
630
631
632
633
634
635
636
637
638
639
640
641
642
643
644

645
646
647
648
649
650

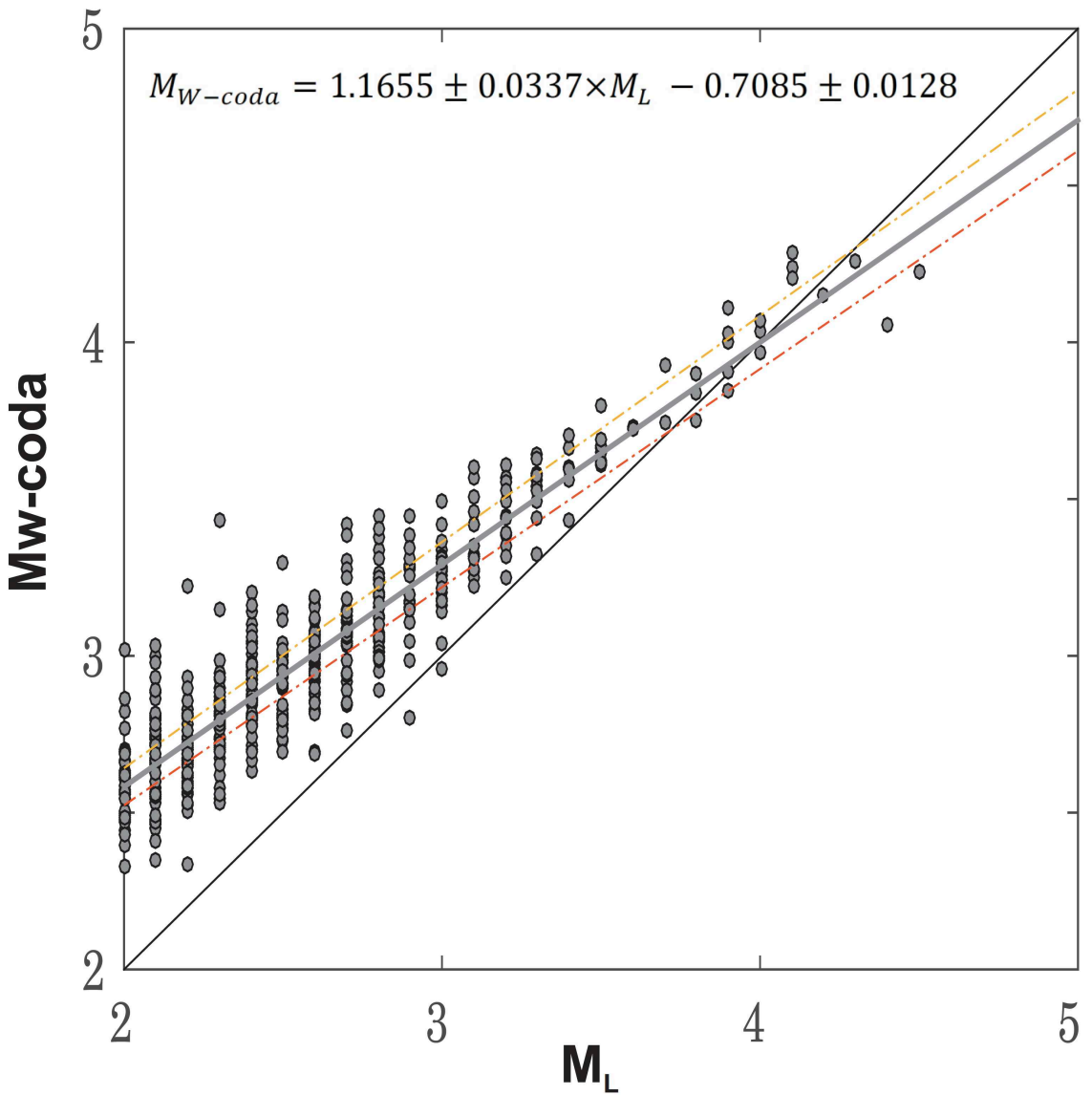
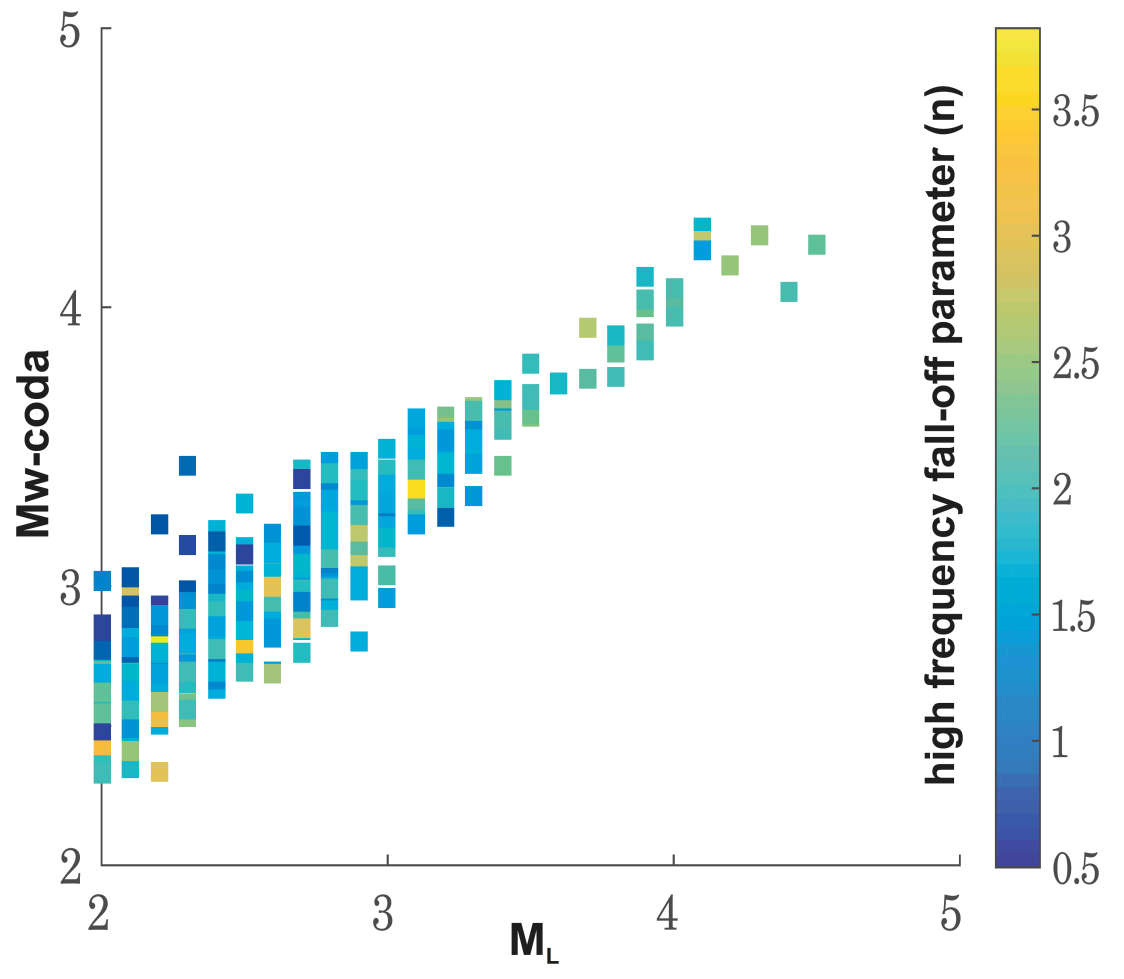


Figure 6.

651
652
653
654
655
656
657
658
659
660
661
662
663
664

665
666



667
668
669
670

Figure 7.